Melt pond conditions on declining Arctic sea ice over 1979–2016: Model development, validation, and results

Jinlun Zhang[1], Axel Schweiger[1], Melinda Webster[2], Bonnie Light[1], Michael Steele[1], Carin Ashjian[3], Robert Campbell[4], and Yvette Spitz[5]

[1]University of Washington

[2]NASA Goddard Space Flight Center

[3]Woods Hole Oceanographic Institution

[4]University of Rhode Island

[5]Oregon State University

June 21, 2018, submitted to *Journal of Geophysical Research*

September 18, 2018, revised

Main 3 points:

(1) A melt pond distribution conservation equation is developed to simulate the evolution of Arctic sea ice melt ponds.

(2) Simulated spatiotemporal variability of melt pond area fraction is generally in good agreement with satellite observations.

(3) Melt pond area and volume on declining Arctic sea ice have changed little during the period 1979–2016.

This article has been accepted for publication and undergone full peer review but has not been through the copyediting, typesetting, pagination and proofreading process which may lead to differences between this version and the Version of Record. Please cite this article as doi: 10.1029/2018JC014298

Abstract

A melt pond (MP) distribution equation has been developed and incorporated into the **M**arginal **I**ce–**Z**one **M**odeling and **A**ssimilation **S**ystem (**MIZMAS**) to simulate Arctic MPs and sea ice over 1979–2016. The equation differs from previous MP models and yet benefits from previous studies for MP parameterizations as well as a range of observations for model calibration. Model results show higher magnitude of MP volume per unit ice area and area fraction in most of the Canada Basin and the East Siberian Sea and lower magnitude in the central Arctic. This is consistent with MODIS observations, evaluated with MEDEA data, and closely related to top ice melt per unit ice area. The model simulates a decrease in the total Arctic sea ice volume and area, owing to a strong increase in bottom and lateral ice melt. The sea ice decline leads to a strong decrease in the total MP volume and area. However, the Arctic-averaged MP volume per unit ice area and area fraction show weak, statistically insignificant downward trends, which is linked to the fact that MP water drainage per unit ice area is increasing. It is also linked to the fact that MP volume and area decrease relatively faster than ice area. This suggests that overall the actual MP conditions on ice have changed little in the past decades as the ice cover is retreating in response to Arctic warming, thus consistent with the MODIS observations that show no clear trend in MP area fraction over 2000–2011.

1. Introduction

Significant decline of Arctic sea ice has been observed in the past decades [e.g., *Cavalieri and Parkinson*, 2012; *Parkinson and Comiso*, 2013]. The decline occurred after years of shrinking and thinning of the ice cover [e.g., *Kwok and Rothrock*, 2009; *Zhang et al.*, 2012; *Meier et al*., 2014; *Lindsay and Schweiger*, 2015], in conjunction with increasing surface air temperature (SAT) [*Hassol*, 2004; *Serreze et al*., 2007; *Richter-Menge et al*., 2016]. Thick multi-year ice has been replaced in recent years by thinner first-year ice [*Nghiem et al*., 2007; *Kwok*, 2007; *Maslanik et al*., 2007] that is more sensitive to changes in atmospheric and oceanic forcing [*Zhang et al*., 2008]. The decline has been particularly steep in summer, when the Arctic sea ice extent and volume decreased to the lowest levels in the satellite era [e.g., *Schweiger et al*., 2011; *Comiso*, 2012; *Meier et al*., 2014]. The decrease in ice extent and volume in late spring and summer has increased the absorption of solar radiation at the ocean surface because of the positive ice–albedo feedback [*Perovich et al*., 2007, 2008], which enhances ice melt and contributes to further ice decline [e.g., *Steele et al*., 2010].

The effect of the positive ice-albedo feedback is further enhanced by the presence of melt ponds (MPs). MPs form on Arctic sea ice during the late spring and summer owing to the accumulation of water from rain and melting snow and ice [e.g., *Perovich et al*., 2002; *Rösel and Kaleschke*, 2012; *Polashenski et al*., 2012; *Liu et al*., 2015; *Han et al*., 2016]. The MPs reduce the surface albedo because pond-covered ice has a lower albedo than bare ice. The surface albedo of MPs is in the range 0.1–0.5 [e.g., *Grenfell and Maykut*, 1977; *Morassutti and LeDrew*, 1996; *Perovich et al*., 2002; *Eicken et al*., 2004], while the surface albedo of bare ice or snow-covered ice is in the range 0.5–0.85 [*Perovich*, 1996; *Grenfell and Perovich*, 2004]. As a result, pond-covered ice absorbs and transmits significantly more incident solar radiation than bare ice [*Nicolaus et al*., 2012; *Light et al*., 2008, 2015]. The greater absorption of solar

energy enhances surface heating and light penetration through the ice cover, thus enhancing bottom and lateral ice melt, elevating water temperature, and increasing the potential for photosynthesis in the water column. The occurrence of the massive under-ice phytoplankton bloom observed in the Chukchi Sea in 2011 was attributed partially to increased penetration of light to the upper ocean through MPs as well as thin, first-year ice [*Arrigo et al*., 2012].

Given the climatic and biological importance of MPs, there have been increasing efforts to develop MP models and incorporate them into large-scale climate and operational forecast models [*Lüthje et al*., 2006; *Flocco and Feltham*, 2007; *Skyllingstad and Paulson*, 2007; *Skyllingstad et al.*, 2009; *Pedersen et al*., 2009; *Flocco et al.*, 2010, 2012, 2015; *Holland et al*., 2012; *Roeckner et al*. 2012; *Hunke et al*., 2013, 2015]. These efforts have improved model representation of MPs. Some of the model studies document the impact of MPs on simulating Arctic sea ice volume and extent [e.g., *Pedersen et al*., 2009; *Flocco et al*., 2012; *Roeckner et al*. 2012]. One model study shows that the simulated MP area fraction (the fraction of sea ice area covered by MPs) in spring is useful for predicting the variations of Arctic sea ice extent minimum in September [*Schröder et al*., 2014]. These model studies, together with various observational studies, have shed considerable light on the behavior of MPs and their influence on the Arctic sea ice mass balance.

However, much remains to be done to fully understand and appropriately model the evolution of MPs in the Arctic. For example, few studies have examined the behavior of MP volume in the Arctic. Unlike MP area, MP volume is more directly related to the energy budget because a gain in MP volume induced by ice and snow melt represents a specific change in the energy balance. MP volume also has a role in modifying freshwater flux at the ocean surface.

This model study focuses on spatiotemporal changes in both MP volume and area, with special attention given to the link between these quantities and ice and snow melt. We present a MP distribution (MPD) conservation equation and incorporated it into the **M**arginal **I**ce **Z**one **M**odeling and **A**ssimilation **S**ystem (**MIZMAS**, *Schweiger and Zhang*, 2015; *Zhang et al*., 2016). We then simulate the changes in MPs as well as Arctic sea ice over 1979–2016, using satellite observations of MP area fraction for model calibration and evaluation. A range of ice concentration and draft/thickness and snow depth observations are also used for model calibration and validation.

After a brief review of the existing MIZMAS sea ice model component in section 2, the MPD equation and related parameterizations are presented in section 3. MIZMAS configuration, forcing, initialization, and simulations are briefly described in section 4, followed by results from model validation and analysis in section 5. Section 5 shows changes in Arctic sea ice and the overlying MPs (sections 5.2 and 5.3) after a description of satellite and in situ observations and a systematic model calibration and validation (section 5.1). The effect of incorporating MPs and model sensitivity to key MP parameters are examined in section 5.4. Concluding remarks are given in section 6.

2. Brief Review of MIZMAS and its Ice Thickness and Snow Distribution Equations

MIZMAS is adapted from the **P**an-arctic **I**ce/**O**cean **M**odeling and **A**ssimilation **S**ystem (PIOMAS*; Zhang and Rothrock,* 2003). MIZMAS differs from PIOMAS in that its displaced pole position is different, allowing for a higher horizontal resolution in the Chukchi, Beaufort, and Bering seas [*Schweiger and Zhang*, 2015]. It is a sea ice–ocean model that assimilates satellite observations of sea ice concentration and sea surface temperature (SST). The sea ice

model component of MIZMAS is a thickness and enthalpy distribution (TED) sea ice model [*Zhang and Rothrock*, 2003; *Hibler*, 1980], with 8 sub-grid categories at each grid cell for ice thickness distribution (ITD), ice enthalpy distribution, and snow distribution (SD), which also differs from the PIOMAS sea ice model that has 12 sub-grid categories. The ocean model component is based on the Parallel Ocean Program (POP, *Smith et al.*, 1992). Detailed information about the sea ice and ocean model components and data assimilation can be found in *Schweiger and Zhang* [2015] and *Zhang et al*. [2016] and are not repeated here.

Before introducing the MPD conservation equation, it is useful to briefly review the *Thorndike et al*. [1975] ITD theory that is implemented in the TED sea ice model. In the ITD theory, the ice mass conservation is described by an ITD conservation equation,

$$\frac{\partial g_h}{\partial t} = -\nabla \cdot (\mathbf{u} g_h) - \frac{\partial (f_h g_h)}{\partial h} + \Psi \,, \tag{1}$$

where g_h is the ITD function, t is time, $\mathbf{u}$ is ice velocity vector, f_h is ice growth rate, h is ice thickness, and Ψ is a mechanical thickness redistribution function for ridging. The thickness redistribution function consists of two terms $\Psi = \Psi_0 + \Psi_r$, which describe the mechanical changes in ITD due to open water creation (Ψ_0) and ridging (Ψ_r) that transfers thin ice to thick ice categories [see *Hibler*, 1980 for details]. As shown in (1), the *Thorndike et al.* ITD theory assumes that changes in the ITD are due to ice advection, thermodynamic growth or decay, lead opening (open water creation), and ridging. The ITD theory is augmented by an ice enthalpy distribution theory to conserve thermal energy of ice [*Zhang and Rothrock*, 2001, 2003]. The TED sea ice model can be used to integrate over multiple sub-grid categories each for ice thickness and ice enthalpy.

The TED sea ice model also includes multiple categories of SD following *Flato and Hibler* [1995]. Changes in SD are described by a SD conservation equation,

$$\frac{\partial(hg_s)}{\partial t} = -\nabla\cdot(\mathbf{u}hg_s) - \frac{\partial(f_h hg_s)}{\partial h} + S_f - S_m - \Psi_r h\frac{g_s}{g_h}, \quad (2)$$

where g_s is the SD function, a function of ice thickness h, such that $hg_s(h)dh$ is defined as the equivalent ice volume per unit area of snow, covering ice of thickness between h and $h+dh$, S_f is the snowfall rate expressed as equivalent ice thickness per unit time, and S_m is the similarly defined snow melt rate. Unlike the ITD function g_h that is a normalized distribution function, g_s is a non-normalized distribution function. The difference between the normalized distribution function g_h and the non-normalized distribution function g_s is that the integration of the former over all ice thickness categories must always be equal to 1 [*Thorndike et al*., 1975] and the integration of the latter may yield values within the range of [0, 1]. According to *Flato and Hibler* [1995], the first term on the right-hand side of (2) describes the advection of snow in the physical space as it is carried along with ice. The second term represents the advection of snow in the ice thickness space as snow is carried along with growing or melting ice that shifts from one thickness category to another. The third term is a source term due to falling snow and the fourth term is a sink term due to snow melt. The last term in (2) represents snow lost to the ocean as ice is ridged [*Flato and Hibler*, 1995].

3. The MPD Equation and MP Parameterization

The successful development and implementation of the SD conservation equation (2) of *Flato and Hibler* [1995] suggests that the MPD conservation equation may be formulated similarly such that

$$\frac{\partial(hg_p)}{\partial t} = -\nabla\cdot(\mathbf{u}hg_p) - \frac{\partial(f_h hg_p)}{\partial h} + R + G - D - F - \Psi_r h\frac{g_p}{g_h}, \quad (3)$$

where g_p is the MPD function such that $hg_p(h)dh$ is defined as the equivalent ice volume per unit area of MPs (also denoted as V_p here), covering ice of thickness between h and $h+dh$. Here, (3) describes changes in MPD brought about by ice advection in the physical space (first term on the right-hand side), ice advection in the ice thickness space due to ice growth or melt (second term), rainfall (R), meltwater growth due to ice/snow melt (G), MP water drainage due to the porosity of sea ice (D), MP water refreezing due to freezing temperature (F), and MP water lost into the ocean due to ice ridging (last term), all expressed as equivalent ice volume per unit area per unit time. The last term in (3) is similar to the last term in (2) and calculated in the same fashion following *Flato and Hibler* [1995]. Like the SD function g_s, the MPD function g_p is also a non-normalized function. The MPD, like the SD as well as the ITD, is described by a single conservation equation, which is solved jointly with the companion SD and ITD equations using the same numerical procedures. In particular, the finite-differencing scheme in the ice thickness space for all three equations is based on Appendix C in *Hibler* [1980]. This differs from the *Flocco and Feltham* [2007] method that represents MPD in a cluster of equations each of which describes the evolution of a single MP category. However, both our approach and that of *Flocco and Feltham* [2007] include changes in MPD due to ice motion and growth or melt, snow melt, rainfall, and MP water drainage etc.

In (3) the rainfall rate R is determined by the atmospheric precipitation forcing of the model. The meltwater growth rate G is determined by (1) and (2), which calculate ice and snow melt rates for each ice thickness category [*Zhang and Rothrock*, 2003; *Hibler*, 1980]. The MP water drainage rate D for each ice thickness category is determined following *Hunke et al*. [2013, 2015]. Meltwater accumulating on top of sea ice has the tendency to drain into the underlying ocean because of the porosity of sea ice. The rate of vertical drainage of MP water through porous sea ice into the ocean is determined by Darcy's law that describes flow through

a porous medium such that [*Hunke et al.*, 2013, 2015, also see *Flocco and Feltham*, 2007; *Flocco et al*., 2010, 2012]:

$$D = -\frac{\Pi_v}{\mu}\rho_o g \frac{\Delta H}{h} d_p, \tag{4}$$

where Π_v is the vertical component of the permeability tensor, μ is the viscosity of MP water, ρ_o is the ocean water density, g is gravitational acceleration, ΔH is the hydraulic head (the height of pond water above sea level), and d_p is a drainage scaling factor. Proposed by *Golden et al*. [2007], detailed information about the formulation of the vertical permeability of sea ice Π_v is given by Eq. (68) in *Hunke et al*. [2015], therefore not duplicated here. Eq. (4) specifies that the drainage rate D over sea ice of thickness (h) is determined by the vertical component of the Darcy velocity (the vertical mass flux per unit area) weighted with a drainage scaling factor d_p. The value of this empirical drainage scaling factor, which controls the magnitude of the drainage rate, is unknown and thus it is a tunable parameter, which is to be determined through model calibration using available satellite MP observations.

The refreezing of MP water is a complicated process [*Flocco et al*., 2015]. Here, for simplicity, the MP water refreezing rate F is determined following the simple approach of *Holland et al*. [2012]. For freezing conditions, *Holland et al*. [2012] use an exponential function of the air temperature to reduce the MP volume,

$$V_p^{i+1} = V_p^i e^{0.01(T_{melt}-T_{sfc}-2)/(T_{melt}-2)}, \tag{5}$$

where V_p is MP volume per unit area as mentioned earlier, the superscript i represents the time step, T_{melt} is the melting temperature for sea ice (set to 0^{o}C), and T_{sfc} is the surface air temperature [*Holland et al*., 2012]. Using the volume of MPs in the equivalent ice volume per unit area, $hg_p(h)dh$, to replace V_p in (5) for a given ice thickness category, we obtain

$$g_p^{i+1} = g_p^i e^{0.01(T_{melt} - T_{sfc} - 2)/(T_{melt} - 2)}. \quad (6)$$

Here (6) describes the effect of MP volume reduction on the MPD function in freezing conditions. The value of –2°C is used to make sure that when surface air temperature is below –2°C, melt ponds would disappear rapidly as the freeze-up progresses [*Holland et al*., 2012].

MPs affect surface albedo and therefore radiative fluxes. Following *Holland et al*. [2012] [also see *Pedersen et al*., 2009], mean surface albedo α and radiative fluxes F for each ice thickness category are given by

$$\alpha = \alpha_i A_i + \alpha_s A_s + \alpha_p A_p \quad \text{and} \quad F = F_i A_i + F_s A_s + F_p A_p, \quad (7)$$

where α_x, A_x, and F_x are albedo, area fraction, and radiative fluxes for bare ice (x = i), snow (x = s), and MPs (x = p), respectively. For a given ice thickness category with area fraction $g_h(h)dh$, we require

$$A_i + A_s + A_p = g_h(h)dh. \quad (8)$$

In this study, the MP albedo α_p (broadband) depends on MP depth and is determined following *Morassutti and LeDrew* [1996]:

$$\alpha_p = 0.177 + e^{(-12.272 h_p - 0.996)}, \quad (9)$$

where h_p is MP depth in meters. Note that MP albedo is also dependent on the thickness of the underlying ice [*Light et al*., 2015]. For simplicity, the effect of ice thickness on MP albedo is not taken into account in this study.

The relationship among the MP depth h_p, area fraction A_p, and volume for a given ice thickness category can be written as

$$h_p A_p = \int h g_p(h)\,dh\,(\rho_i/\rho_w), \quad (10)$$

where ρ_w and ρ_i are meltwater and ice densities, respectively. Based on a linear fit to the observed SHEBA (Surface Heat Budget of the Arctic Ocean) time evolution of MP area fraction and depth [*Perovich et al*., 2003], *Holland et al*. [2012] propose a relationship between the MP depth and area fraction such that $h_p = 0.8A_p$. While this relationship simplifies the solution of (10), it neglects the effect of ice thickness on MP depth h_p and area fraction A_p. Observations indicate that thick or multi-year ice tend to have deeper MPs than thin or first-year ice [*Morassutti and LeDrew*, 1996]. Thus we propose a modification to the *Holland et al*. [2012] relationship, such that

$$h_p = 0.8A_pK_p, \quad (11)$$

where K_p is a MP depth factor given as

$$K_p = \begin{cases} 1, & \text{if } h \le 2\text{m} \\ \max(1, C_h h), & \text{otherwise} \end{cases}, \quad (12)$$

where C_h is an ice thickness scaling factor. We note that if C_h is set to be $1/h$ as a special case, then the MP depth factor K_p is always equal to 1 and the relationship between the MP depth and area fraction is identical to that in *Holland et al*. [2012]. If the ice thickness scaling factor C_h is set to be a constant between 0 and 1, then for ice of thickness ≤ 2 m, (11) is identical to the *Holland et al*. [2012] relationship. However, for ice of thickness > 2 m, MP depth can increase with the thickness of the underlying ice, as reflected in observations [e.g., *Morassutti*

and LeDrew, 1996]. The rate of increase in MP depth on ice of given thickness is controlled by the currently unknown empirical constant C_h, which is determined through model calibration. In addition, the model limits the value of MP depth to be less than 90% of ice thickness, which is also based on *Holland et al*. [2012]. This means that the model does not allow MPs to melt through the ice unless the ice in that cell is completely melted.

4. Model Setup and Calibration

4.1. Model configuration, forcing, and initialization

The model domain of MIZMAS, based on a generalized orthogonal curvilinear coordinate system, covers the Northern Hemisphere north of 39°N, consisting of the Arctic, North Pacific, and North Atlantic oceans [see Figure 1a in *Schweiger and Zhang*, 2015]. The model was integrated from 1979 to 2016, driven by daily surface atmospheric forcing from the NCEP Climate Forecast System (CFSv2, *Saha et al*., 2014) (over 2011–2016) and the equivalent Climate Forecast System Reanalysis (CFSR, *Saha et al*. 2010) (over 1979–2010). Transition between these two data sets appears to not affect sea ice results. Atmospheric forcing includes surface air temperature (at 2 m), winds (at 10 m), downwelling shortwave and longwave radiation, specific humidity, precipitation, and evaporation. Note that the CFSR/CFSv2 reanalysis forcing is not available before 1979. To obtain initial conditions for the integration, the model was integrated from 1972 to 1978 without incorporating MPs, driven by daily NCEP/NCAR reanalysis [*Kalnay et al*., 1996] atmospheric forcing [see *Schweiger and Zhang*, 2015 for details]. The sea ice and ocean conditions at the end of 1978 were then used as initial conditions for the 1979–2016 integration with MPs incorporated. The use of the CFSR/CFSv2 reanalysis forcing for the 1979–2016 integration is based on the study of *Lindsay et al*. [2014] that reports the CFSR/CFSv2 downwelling shortwave radiation has a smaller bias than the NCEP/NCAR reanalysis in summer.

The integration over 1979–2016 was first calibrated using a range of available satellite and in situ observations. The calibration process involves a series of calibration runs over 1979–2016. During the calibration runs, the empirical constants d_p in (4), which controls MP drainage, and C_h in (12), which determines how MP depth changes for thick ice, are estimated by varying their values and by comparing the results with available MP area fraction derived from MODIS (Moderate Resolution Imaging Spectroradiometer) over the period 2000–2011 (see section 5.1) [*Rösel et al.*, 2012]. By subjectively comparing the 2000–2011 mean seasonal cycle and the July 2000–2011 mean map of MP area fraction with MODIS observations, we selected the following values: $d_p = 0.015$ and $C_h = 0.75$. Meanwhile the albedo parameter for melting bare ice is also adjusted in order to reduce mean ice thickness bias in comparison with all available observations of ice draft/thickness over the period 1979–2014 (also see section 5.1). We adopted a value of 0.58 for the albedo parameter after calibration (Table 1). Also listed in Table 1 are other prescribed albedo parameters. MP albedo, α_p, is not listed in Table 1, because it is computed based on (9). Note that in the case that MP water is completely drained with h_p reduced to zero, α_p is equal to 0.55. This means that the albedo of bare ice at the bottom of the newly drained MPs is slightly lower than that of the general melting bare ice (0.58). Once the fraction of the newly drained MP is added to the fraction of existing bare ice, the value of albedo becomes 0.58, for both the existing and the newly converted bare ice.

SST assimilation in MIZMAS is based on *Manda et al*. [2005] and is performed only in the open water areas where satellite observations are available [also see *Zhang et al*., 2016]. Ice concentration assimilation is based on *Lindsay and Zhang* [2006], allowing for two options: (i) assimilation over the entire ice-covered areas or (ii) only near the ice edge. In this study, option (ii) is chosen. This means that the assimilation is performed only in the areas where

either model or satellite ice concentration is below 0.15 (defined here as open water areas; 0.15 ice concentration defined as ice edge). In other words, no assimilation is conducted in the areas where both model and satellite ice concentrations are at or above 0.15. This approach forces the simulated ice edge close to observations, while allowing us to assess the simulated behavior of freely evolving MPs and other sea ice variables in ice-covered areas without constraints by observations.

4.2. Satellite MP data and comparison

MIZMAS is calibrated and validated using available MP area fraction data derived using MODIS images over the period 2000–2011. These MP area fraction data are obtained from MODIS visible channels 1, 3, and 4 using a neural network inversion algorithm that assumes spectral properties for endmembers of open water, sea ice, and MPs in 500-m spatial resolution [*Rösel et al.*, 2012]. We obtained the data from the web site (https://icdc.cen.uni-hamburg.de/1/daten/cryosphere/arctic-meltponds.html), which provides fractions for open water and MPs per unit (grid) area gridded at 12.5-km resolution and 8-day intervals from May through September over 2000–2011. The MP fraction per unit area can be converted to MP fraction per unit ice area (or MP area fraction for simplicity) by normalization with (i.e., dividing by) ice concentration.

MODIS MP area fractions were also compared with those derived from National Technical Means images, referred to hereinafter as MEDEA images [*Kwok and Untersteiner,* 2011; http://gfl.usgs.gov/]. The MEDEA images are radiometrically inconsistent, grayscale images with 1-m spatial resolution and typically cover a 15×15-km to 30×30-km domain [*Kwok and Untersteiner*, 2011]. The MEDEA MP area fractions were derived following *Webster et al.* [2015], which combines geophysical and proximity relationships with pixel

intensities to distinguish MPs from sea ice, thin ice, and open water. The average accuracy for the May–September segmentations in *Webster et al.* [2015] was 98%.

There are 36 MP area fractions derived from 36 MEDEA images (Figure S1 in Supplementary Information) overlapping with the MODIS data. Because the MODIS data set provides an 8-day composite and a MEDEA image provides an instantaneous value, the following matchup procedure is used. For each MEDEA image we find the 8-day MODIS interval that contains the MEDEA acquisition time and extract all MODIS grid cells that fall within the area covered by the MEDEA image. Other matchup procedures were explored, but yielded similar results.

The MODIS MP area fractions compare well with the available MEDEA data (Figure 1), with a high correlation of R = 0.85 and a positive bias of 5.6%. This correlation value is higher than that reported by *Rösel et al*. [2012] (R^2 = 0.28 or R = 0.53) using similar input data based on the MEDEA images but processed with a different algorithm [*Fetterer and Untersteiner,* 1998; *Fetterer et al*., 2008]. The *Rösel et al*. [2012] study also reports a positive bias in MODIS data relative to the high-resolution MEDEA data, but no bias relative to surface measured MP area fraction. These prior results, together with Figure 1, indicate that MODIS captures the temporal and spatial variability of MP area well and is therefore suitable for model calibration and validation.

5. Results

5.1. Comparisons with observations: MP area fraction, ice concentration, ice draft/thickness, and snow depth

The spatial pattern of the MODIS-derived July mean MP area fraction, averaged over 2000–2011, is characterized by generally higher values in most of the Canada Basin and the East Siberian Sea and lower values in the central Arctic, outside of the North Pole region where MODIS observations are not available, and in some areas near the Canadian Archipelago and northern Greenland (Figure 2a) [also see *Rösel et al*., 2012]. Model results generally agree with this spatial pattern (Figure 2b), especially in most of the Canada Basin and the East Siberian Sea. However, the model overestimates MP area fraction in most of the central Arctic and near ice edges. The overall mean model bias is rather low, only 1.6% (against an observed mean value of 21.0%), based on a model–MODIS comparison using the MP area fraction averaged weekly during May–August of 2000–2011 over the Arctic Ocean (Figure 3a). (The Arctic Ocean is here defined as the area north of 66.6^{o}N). In addition, the model results are highly correlated with the MODIS observations (R = 0.92), indicating that the model captures ~85% of the variance of the observations.

MIZMAS also reproduces most of the seasonal variations of the MODIS-derived MP area fraction averaged over the Arctic Ocean (Figure 3b). Both MODIS and MIZMAS show that MP area fractions are generally small in May, climb rapidly in June, and peak in late July or early August before descending. From May to August, the model simulated weekly MP area fractions stay close to the MODIS observed values or within the variation range (standard deviation) of the observations. After peaking, the simulated area fractions decrease at a faster pace than the MODIS observations and drop out of the variation range of the observations in September (Figure 3b). This deviation may be an indication of model deficiency at a time when the MP season is winding down, suggesting that (5) may not represent MP refreezing processes well. On the other hand, observational uncertainties may increase after peak pond coverage due to the misclassifications of brash ice, rotten ice, etc. as MPs [*Webster et al*., 2015].

MIZMAS tends to overestimate ice concentration in much of the marginal ice zone during June–September when compared to satellite observations (Figure S2). However, in the interior of the ice pack, MIZMAS underestimates ice concentration, particularly in August. MIZMAS is further evaluated using available sea ice (mean) draft or thickness observations from various sources collected over the period 1979–2014 (Figures S3a–b). These observations are obtained from the Unified Sea Ice Thickness Climate Data Record (CDR) [*Lindsay*, 2010; 2013] (also see http://psc.apl.uw.edu/sea_ice_cdr), which provides 4,309 observations over 1979–2014 (Figure S3a). The model tends to underestimate ice draft (thickness) in the central Arctic, while the opposite is true for the Beaufort Sea (Figure S3b). This bias is common in many sea ice models [*Johnson et al*., 2012]. Overall, the comparison shows a mean bias of 0.03 m (1.2% relative to an observed mean value of 2.59 m), although some individual points may show discrepancies of up to several meters (Figure S3a). The model–observation correlation is R = 0.72, suggesting that the model captures more than 50% of the variance of the observations.

Snow depth data collected by the NASA Operation IceBridge mission (N = 1,364 data points) during March–April of 2009–2015 [Versions 1 and 2, *Kurtz et al.,* 2013] are compared with model results (Figures S3c–d). The model tends to underestimate snow depth in the areas near the Canadian Archipelago and overestimate it in North Pole and Fram Strait region (Figure S3d). Overall, the model has a mean bias of 0.02 m (or 9.3% relative to an observed mean value of 0.22 m), with a model–observation correlation of R = 0.56 (Figure S3c).

5.2. Declining Arctic sea ice in summer with widespread MPs

The model simulated decline of summer Arctic sea ice is reflected in the steady decrease of both the total ice volume and area, superposed with considerable interannual fluctuations (Figures 4a–b; Table 2). The percentage downward trend of ice volume is higher than that of ice area (Table 2), which is not surprising given that the ice cover has been thinning and shrinking concurrently. The decline of sea ice is also evident over an earlier period (1979–1997) and a later period (1998–2016; Figures S4a–d). The decline is also reflected in the seasonal evolution with ice volume lower during the later period 1998–2016 in all seasons, while ice area has a stronger decline during the summer months (Figures 5a–b).

During the later period 1998–2016, ice melt increased throughout the melting season, in response to Arctic warming [e.g., *Richter-Menge et al*., 2016]. Ice growth increased as well during November through December (Figure 5c) because a thinner ice and snow cover, tends to accelerate ice growth in fall and winter [*Maykut*, 1982; *Bitz and Roe*, 2004]. However, they do not compensate and the annual net ice production during 1998–2016 is lower than that during 1979–1997, leading to a thinner and less compact ice cover in the later period (Figure S4).

The increase in ice melt is further reflected in the positive trend over the period 1979–2016 (Figure 4c; Table 2). Ice melt (also referred to as total ice melt here for clarity) consists of melt at the top, bottom, and lateral sides of the ice. The simulated increase in the total melt is not due to an increase in the top melt. The simulated June–August mean top melt, which contributes to the formation of MPs, actually decreases over 1979–2016, although the downward trend is not statistically significant (Figure 4c; Table 2) when accounting for temporal autocorrelation [e.g., *Santer et al*., 2000]. The statistically insignificant decrease is also illustrated in the spatiotemporal changes in the top melt (Figure 6). The simulated top melt

field in June is generally higher in the Chukchi, Beaufort, and East Siberian seas than in the rest of the Arctic, particularly the central Arctic (Figures 6a and 6d). In July, higher top melt spreads into much of the Arctic Basin (Figures 6b and 6e), similar to that reported by *Steele et al*. [2010]. Top melt then declines in August, with a steeper decrease in the central Arctic (Figures 6c and 6f). During 1998–2016, the simulated top melt is generally lower than the earlier period 1979–1997 throughout summer, a result of decreasing ice area and hence increasing open water area in the Arctic (Figure 4b).

The increase in the total melt is in fact due to an increase in the combined bottom and lateral melt, a result of ocean heat increase (Figure 4c), occurring mostly near the ice edge and in the marginal ice zone where ice is relatively thin and less compact (Figure 7; also see *Tsamados et al*., 2017). Throughout summer, it is much higher and more widespread in the later period than the earlier period. As a result, the simulated bottom and lateral melt has the largest relative upward trend (1.82% yr^{-1}) among all the variables (Table 2). This confirms that the decrease in ice volume and area, together with the existence of MPs, allows elevated absorption of solar energy at the ocean surface because of the positive ice-albedo feedback [e.g., *Perovich et al*., 2007, 2008], which warms the ocean waters and thereby enhances bottom and lateral melt. While bottom and lateral melt does not provide meltwater to MPs, it contributes to an overall upward trend in the total melt and therefore the accelerated summer ice retreat, which in turn has an impact on MP volume and area (see section 5.3). On the other hand, MPs tend to increase bottom and lateral melt by allowing more sunlight to penetrate through the ponded ice cover.

In addition to ice volume, the simulated snow volume in the Arctic also decreases over 1979–2016 (Figure 4d; Table 2). Snow volume peaks in May before mostly melting away in

July and August, and is lower all year round in the later period than the earlier period (Figure 5d). The decrease in snow depth occurs in most of the Arctic (Figures S4e–f), consistent with *Webster et al*. [2014] for the western Arctic. Because of the decrease in snow volume, the amount of snow melt also decreases, as expected (Figure 4d; Table 2). In contrast to the decrease in top ice melt, the decrease in snow melt is statistically significant (Table 2). However, the rate of snow melt is much smaller than that of top ice melt (Figures 4c–d), particularly in terms of meltwater equivalent, given that the snow density (330 kg m^{-3}) is much lower than ice density (910 kg m^{-3}). Thus, while snow melt affects the formation of MPs, top ice melt plays a more prominent role as a water supplier to MPs and is examined further in the next section.

5.3. Changes in MPs on declining Arctic sea ice

In section 4.2, we described the difference between two variables related to MP area: the MP fraction per unit (grid) area or simply MP fraction per unit area and MP fraction per unit ice area or simply MP area fraction. For MP volume, we define similar quantities, i.e., MP volume per unit (grid) area or simply MP volume per unit area and MP volume per unit ice area. MP volume per unit area [(defined by $V_p = (\rho_i/\rho_w) \int_0^\infty g_p(h)hdh$), an integration over all ice thickness categories; see (3)] is an average over combined open water and ice areas of different thickness categories. MP volume per unit area, like MP fraction per unit area, is a useful variable to describe the state of MPs and their freshwater content within a given area regardless of ice conditions. However, MPs are on top of ice and the actual MP volume depends on ice conditions. The actual MP volume on ice or MP volume per unit ice area, like MP area fraction, needs to be normalized (i.e., divided) by ice concentration. The definition of per unit

(grid) area or per unit ice area also applies to other variables, such as snow depth, top ice melt, and MP water loss (see below).

Because of the thinning and shrinking of the Arctic sea ice cover and the associated decrease in top ice melt and snow melt during 1979–2016, it is not surprising that the model simulates a steady decrease in the total MP volume and area, which are calculated by integrating MP volume per unit area and MP fraction per unit area over the Arctic Ocean (Figures 4a–b). The summer mean MP volume is about 5% of the summer mean ice volume, whereas the MP area is about 25% of the ice area (Table 2). The percentage downward trends (relative to the means) in MP volume and area are all slightly greater than those in ice volume and area (Table 2), suggesting that when ice volume and area are decreasing, MP volume and area may tend to decrease slightly faster. Seasonally, the simulated MP volume peaks in July (Figure 5e), while the simulated MP area peaks either in July or August (Figure 5f). Changes in MP volume and area are small in June and September between the 1979–1997 and 1998–2016 periods. However, MP volume and area are lower in July and August in the later period (Figures 5e–f).

The decrease in MP volume is further reflected in the simulated fields of MP volume per unit area V_p (Figure 8). MP volume per unit area starts to grow in June in the Pacific Arctic, mostly in the Chukchi, Beaufort, and East Siberian seas, while it is lower in much of the Atlantic Arctic (Figures 8a and 8d). This corresponds well to top ice melt in June that shows a similar spatial pattern (Figures 6a and 6d). In July, MP volume per unit area increases in much of the Arctic Basin (Figures 8b and 8e), in conjunction with strong top melt almost everywhere (Figures 6b and 6e). The increase in MP volume per unit area is most prominent in the areas near the Canadian Archipelago and northern Greenland. This is because the ice cover there is

generally more compact (Figures S4c–d) and therefore has more ice area to hold MPs. The ice cover there is also thicker (Figures S4a–b) and therefore less susceptible to the draining of MP water [see (4)]. Thus, MPs hold more freshwater in the areas near the Canadian Archipelago and northern Greenland than in the other areas of the Arctic. In August, MP volume per unit area starts to decrease (Figures 8c and 8f) as the ice becomes more porous and the top ice melt lessens (Figures 6c and 6f). Throughout summer, MP volume per unit area in much of the Arctic is generally less in the later period (Figure 8), in association with generally less top ice melt (Figure 6) as well as snow melt (not shown).

The fields of MP volume per unit ice area (Figure 9) differ strikingly from those of MP volume per unit area (Figure 8), the latter being independent of ice conditions. The spatiotemporal differences between these two variables are due to the spatiotemporal changes in ice concentration (Figures S4c–d). As expected, MP volume per unit ice area is higher in magnitude than MP volume per unit area, because of the normalization with ice concentration. Both have a similar spatial pattern in June, with higher magnitudes in parts of the Pacific Arctic than in the Atlantic Arctic (Figures 8 and 9). However, in July and August, MP volume per unit ice area continues to be high in parts of the Pacific Arctic, even though greater MP volume is simulated in the areas near the Canadian Archipelago and northern Greenland as reflected in the fields of MP volume per unit area (Figure 8). This means that MP volume on ice is actually higher in parts of the Pacific Arctic, where ice is less compact, than in the areas near the Canadian Archipelago and northern Greenland, where ice is more compact. MP volume on ice in July and August is also greater in the Pacific Arctic than in the Atlantic Arctic (Figure 9).

The spatial pattern of MP volume per unit ice area (Figure 9) resembles that of the observed (MODIS; Figure 2a) and model simulated MP area fraction (Figure 10; Figure 2b),

with relatively high magnitude in parts of the Pacific Arctic and low magnitude in the central Arctic and some areas near the Canadian Archipelago and northern Greenland. This spatial pattern may be explained by normalizing the top ice melt per unit area by ice concentration (Figure 11). In contrast with top ice melt (per unit area) (Figure 6), top ice melt per unit ice area for July and August shows a strong spatial gradient, with much higher magnitude in the peripheral seas and marginal ice zone, particularly in the Pacific Arctic, and lower magnitude in the central Arctic, especially in the areas near the Canadian Archipelago and northern Greenland. Although statistically insignificant over the period 1979–2016, the Arctic-averaged top ice melt (per unit area) is decreasing (Figure 4c; Table 2), resulting from the decreasing ice area, while the Arctic-averaged top ice melt per unit ice area is increasing (Figure 12a; Table 2), because the ice is exposed to a generally warmer Arctic environment in the later period. Meanwhile, the Arctic-averaged MP water loss, in association with drainage due to ice porosity and loss due to ice ridging, per unit ice area is increasing (Figure 12b; Table 2), reflecting a thinner ice cover that moves faster and deforms more [e.g., *Rampal et al*., 2009; *Zhang et al*., 2012]. Although also statistically insignificant, the simulated upward trend in MP water loss per unit ice area is slightly greater than that in top ice melt per unit ice area (Table 2).

Simulated total MP volume and area decrease over 1979–2016 (Figure 4; Table 2), which is also reflected in the decrease in MP volume per unit area in most of the Arctic (Figure 8). However, a decrease in MP volume per unit ice area as well as MP area fraction occurs only in the Pacific Arctic in August (Figures 9 and 10). In fact, the simulated Arctic-averaged MP volume per unit ice area and MP area fraction (per unit ice area) display a weak decrease over 1979–2016 (Figures 12c–d; Table 2). The weak decrease in these two variables, which are normalized by ice concentration (area), occurs because the simulated upward trend in MP water loss per unit ice area is slightly greater than the upward trend in top ice melt per unit ice area

(Table 2). The weak decrease is also linked to the fact that the simulated percentage downward trend of ice area (–0.88%) is close to but less than those of MP volume (–1.40%) and area (–0.93%) (Table 2). The downward trends in MP volume per unit ice area and MP area fraction are so small that they are not statistically significant (Table 2). This is why there is very little difference in the seasonal evolution of MP volume per unit ice area and MP area fraction between the 1979–1997 and 1998–2016 periods (Figures 5g–h). The statistically insignificant downward trend is also in line with the MODIS observations of MP area fraction, which show no clear trend over 2000–2011 (Figure 12d). This indicates that the overall MP conditions on ice have changed little over the past few decades, even though the total MP volume and area have been steadily decreasing on a thinning and shrinking ice cover associated with Arctic warming.

5.4. Model sensitivity

The results discussed up to this point are from a model run that is considered a 'control' simulation (denoted hereafter as CNTL). In addition, three sensitivity simulations are conducted in parallel to the CNTL run over the period 1979–2016. These sensitivity runs are aimed at examining the effect of incorporating MPD and model sensitivity to the parameterizations of the drainage scaling factor d_p in (4) and the ice thickness scaling factor C_h in (12) (Table 3). Like the CNTL run, the first two sensitivity runs (SEN1 and SEN2) incorporate MPD. Model sensitivity to d_p described in (4) is represented by two different d_p values (CNTL vs. SEN1). Model sensitivity to ice thickness scaling factor C_h described in (12) is explored by setting C_h to be a constant for CNTL and $1/h$ for SEN2 (Table 3). As described by (12), C_h is normally a constant. Setting C_h to be $1/h$ in SEN2 results in a relationship between the MP depth and area fraction that is identical to that in *Holland et al.* [2012]. The third

sensitivity run (NoMP) does not incorporate MPD and is used to assess how model results differ with and without simulating MPs (CNTL vs. NoMP). All model runs employ the same set of albedo parameters (Table 1) in addition to the MP albedo parameterization given in (9).

The CNTL simulated spatiotemporal variations of MP area fraction compare well with those of the MODIS observations over 2000–2011 (Figures 2 and 3; also see Figure 13a). With an increased drainage scaling factor d_p in the SEN1 run, the simulated July mean MP area fraction (Figure 13b) is lower than the corresponding MODIS observations and the CNTL results throughout the Arctic. The simulated June–August mean total MP volume and area are lower as well over the period 1979–2016 (Figures 14a–b) because enhanced drainage of MP water associated with the increased drainage scaling factor d_p [see (4)] leads to reduced MP volume and area. The reduced MP volume and area result in a slight increase in mean surface albedo, averaged over all surface conditions, and hence a slight decrease in the Arctic-averaged top ice melt (per unit area) (Figures 14c–d). The slight decrease in top ice melt causes a negligible increase in the total summer mean ice volume (Figure 14e) and April–June mean snow volume (Figure 14f) over the CNTL run.

In contrast, the SEN2 run, using the relationship between MP depth and area fraction based exactly on *Holland et al*. [2012], creates much higher MP area fractions than the MODIS observations and CNTL results (Figure 13c). Also, the spatial pattern of the SEN2 simulated MP area fraction disagrees with the MODIS observations of low magnitude in the central Arctic and some areas near the Canadian Archipelago and northern Greenland. The disagreement lies in the fact that when C_h is set to be $1/h$ and hence K_p is always equal to one in (4), thick ice is not allowed to hold more melt or rain water, and melt or rain water can spread out on thick, ridged ice just as easily as thin, level ice, leading to substantially higher MP area

coverage on ice than the CNTL run (Figures 13 and 14b). In contrast, the SEN2-simulated MP volume increase over the CNTL run is small (Figure 14a), because both CNTL and SEN2 runs use the same value for the drainage scaling factor d_p (Table 3), which controls the rate of MP water drainage. Nevertheless, the substantial increase in MP area fraction in the SEN2 run leads to a sizable decrease in surface albedo and increase in top ice melt (Figures 14c–d), which, in turn, results in a decrease in ice and snow volumes (Figures 14e–f). Increasing top melt causes little increase in MP volume because of increased MP water drainage on a thinner ice cover.

The third sensitivity run, NoMP is useful for highlighting the effect of model incorporation of MPD on the ice and snow mass balance. NoMP tends to simulate considerably higher mean surface albedo and lower top ice melt because of the absence of MPs (Figures 14c–d). The higher surface albedo also results in a lower bottom and lateral melt (not shown), as it reduces solar energy input at the ocean surface. The lower top, bottom, and lateral melt leads to greater ice and snow volume (Figures 14e–f). On average over 1979–2016, the increase in the total summer ice volume of NoMP over CNTL is 15%, while the increase in the total April–June mean snow volume is 12%.

6. Concluding Remarks

We have developed a MPD conservation equation and incorporated it into MIZMAS to simulate the evolution of MPs. The MPD conservation equation describes changes in MPD, a non-normalized function, due to ice advection in the physical and ice thickness space, rainfall, ice/snow melt, MP water drainage and refreezing, and loss of MP water induced by ice ridging. The MPD equation is developed based on the methods *Flato and Hibler* [1995] used to develop the SD conservation equation used in MIZMAS. While the MPD equation differs from those

used in previous model studies, some of the key MP parameterizations benefit from those studies, such as the parameterizations of MP water draining and refreezing and the relationship between MP depth and area fraction, which simplifies the solution of the equation (see section 3). The simplification leads to two parameters that need to be specified to close the equation: the drainage scaling factor d_p in (4) and the ice thickness scaling factor C_h in (12), which control the magnitude and spatial pattern of MPs and need to be calibrated to obtain realistic results.

The MPD development in MIZMAS also benefits from satellite and in situ observations used for model calibration and validation; these ensure that the model is generally in good agreement with observations of ice thickness and snow depth, as well as MP area fraction. The model, by calibrating d_p and C_h, generally captures the MODIS observed spatiotemporal variations of MP area fraction over 2000–2011, with low mean model bias and high model–MODIS correlation. Model results show higher magnitudes of MP volume per unit ice area and MP area fraction in most of the Canada Basin and the East Siberian Sea and lower magnitudes in the central Arctic and some areas near the Canadian Archipelago and northern Greenland. This pattern is consistent with MODIS observations and is linked to the spatiotemporal variations of top ice melt per unit ice area.

The well-known decline of Arctic sea ice is seen in the modeled decrease of the total ice volume and area over the period 1979–2016, particularly in summer when MPs are widespread. The decreases in ice volume and area are linked to an increase in the combined bottom and lateral ice melt induced by elevated absorption of solar energy at the ocean surface associated with a positive ice-albedo feedback. The increases in the bottom and lateral ice melt are so great that the total ice melt increases even though top ice melt (per unit area) decreases. The decrease in top ice melt, a major contributor to the formation of MPs, is hardly unexpected,

given the decrease of ice area. In other words, less ice is present and thus less top melt occurs now than decades ago when a greater area was ice-covered during the Arctic melt season. However, the decrease in top ice melt is so weak that its downward trend is statistically insignificant. This is because of the generally warming Arctic environment that tends to boost melt at the ice surface, i.e., increasing top ice melt per unit ice area. The combined effects of increasing top ice melt per unit ice area and decreasing ice area available for top melt result in a weak downward trend in top ice melt (per unit area).

The model shows strong deceases in the total MP volume and area on the declining Arctic sea ice cover over 1979–2016. The thinning and shrinking of the ice cover, in conjunction with the decrease in top ice melt and snow melt, result in decreases in MP volume and area. Results indicate that as Arctic ice volume and area decrease, MP volume and area decrease slightly faster. However, while the total MP volume and area are decreasing strongly, the simulated Arctic-averaged MP volume per unit ice area and MP area fraction show weak, statistically insignificant downward trends over 1979–2016. This is because, with a thinner and more mobile ice cover, the Arctic-averaged MP water loss (drainage due to ice porosity and ice ridging) per unit ice area is increasing and this increase is slightly greater than that of the Arctic-averaged top ice melt per unit ice area. Overall the actual MP conditions on ice have changed little in the past decades while the sea ice cover has thinned and shrunk in response to Arctic warming, which is consistent with the MODIS observations that show no clear trend in the Arctic-averaged MP area fraction over 2000–2011. The lack of a significant trend in melt pond conditions was also found in the sensitivity experiments in which MP parameters were changed. MPs markedly increase the light penetration through ice and therefore have an important role in under-ice blooms [e.g., *Arrigo et al.*, 2012]. Because the overall MP characteristics on ice have not changed fundamentally, the overall behavior of under-ice

blooms is not likely to have undergone significant change in response to MP conditions and such blooms have been consistent occurrences in the Arctic Ocean prior even to recent dramatic declines in sea ice extent and volume [e.g., *Lowry et al*., 2014].

The lack of significant trends in MP volume per unit ice area and MP area fraction over 1979–2016 differs from *Schröder et al*. [2014] that reports a substantial increase in MP area fraction over the period 1979–2013. Is this discrepancy due to model differences in dealing with the competing effect of increasing top melt vs. increasing MP drainage because of decreasing ice thickness and increasing ice porosity? Note that the modeling approach of *Schröder et al*. [2014] differs from ours [*Zhang and Rothrock* 2003] for many aspects of the sea ice–snow system in which MPs are a component. Thus, is this discrepancy due to model differences in dealing with sea ice dynamics/thermodynamics or the interaction between MP processes and other sea ice–snow processes? Addressing these questions requires detailed model analyses and comparisons that are beyond the scope of the present study. We point out the discrepancy to suggest that there are significant uncertainties in model representation of the spatiotemporal variations of MPs in the Arctic. There may be significant uncertainties in model parameterization of MP and other sea ice–snow physical processes, likely due to our knowledge gaps about the processes. Further studies are warranted, via fieldwork and modeling, to enhance our understanding and build a consensus on changes in MPs on the declining Arctic sea ice.

Finally, we want to point out some areas for further model improvement. It is expected that MP albedo depends on the depth of the pond and, perhaps more critically, on the optical properties and the thickness of the underlying ice [e.g., *Perovich et al*., 2002; *Light et al.*, 2015]. Thus the parameterization of MP albedo needs to be refined to include specifically the effect

of MP depth and ice thickness, especially for thinner ice types later in the summer. The improvement in the parameterization of MP albedo may be achieved through seasonal observations of albedo, melt pond area and depth, and sea ice thickness on different sea ice types. Fieldwork may also provide guidance in refining the drainage scaling factor d_p (4) and ice thickness scaling factor C_h (11 and 12), which are determined through numerical experiments in this study. In addition, the model simulated seasonal evolution of MP area fractions differs considerably from that of the MODIS observations in late summer and early fall. This difference may indicate the inadequacy in using (6) to simulate the processes of MP refreezing. Thus it is essential to enhance our understanding of and ability to represent the complicated MP refreezing processes [e.g., *Flocco et al*., 2015] through observations and model development. Additional attention for further model improvement may be placed on the effect of MPs on other processes such as surface sensible and latent heat fluxes, surface momentum exchange [see *Lüpkes et al*., 2013], and ice–ocean freshwater exchange.

Acknowledgments. We gratefully acknowledge the support of the NASA Cryosphere Program (grants NNX15AG68G, NNX17AD27G, and NNX14AH61G), the Office of Naval Research (N00014-12-1-0112), the NSF Office of Polar Programs (PLR-1416920, PLR-1603259, PLR-1602521, and ARC-1203425), and the Department of Homeland Security (DHS, 2014-ST-061-ML-0002). The DHS grant is coordinated through the Arctic Domain Awareness Center (ADAC), a DHS Center of Excellence, which conducts maritime research and development for the Arctic region. The views and conclusions in this document are those of the authors and should not be interpreted as representing the official policies, either expressed or implied, of the DHS. MODIS-derived MP area data are available at https://icdc.cen.uni-hamburg.de/1/daten/cryosphere/arctic-meltponds.html. MP area fraction statistics derived from MEDEA images are available from http://psc.apl.uw.edu/melt-pond-data/ Sea ice

thickness and snow observations are available at http://psc.apl.washington.edu/sea_ice_cdr. CFS forcing data used to drive MIZMAS are available at https://www.ncdc.noaa.gov/data-access/model-data/model-datasets/climate-forecast-system-version2-cfsv2.

References

Arrigo, K.R., and others (2012), Massive phytoplankton blooms under Arctic sea ice. *Science* 336, 1408.

Bitz, C. M., & Roe, G. H. (2004), A mechanism for the high rate of sea ice thinning in the Arctic Ocean. *Journal of Climate, 17*(18), 3623-3632.

Eicken, H., T. C. Grenfell, D. K. Perovich, J. A. Richter-Menge, and K. Frey (2004), Hydraulic controls of summer Arctic pack ice albedo, *J. Geophys. Res., 109*, C08007, doi:10.1029/2003JC001989

Fetterer, F., and N. Untersteiner, Observations of melt ponds on Arctic sea ice (1998), *J. Geophys. Res., 103*, 24,821–24,835.

Fetterer, F., S. Wilds, and J. Sloan (2008), Arctic sea ice melt pond statistics and maps, 1999–2001, Digital Media (ftp), http://nsidc.org/data/g02159.html.

Flato, G.M., and W.D. Hibler III (1995), Ridging and strength in modeling the thickness distribution of Arctic sea ice. *J. Geophys. Res., 100*, 18,611–18,626.

Flocco, D., and D. L. Feltham (2007), A continuum model of melt pond evolution on Arctic sea ice, *J. Geophys. Res., 112*, C08016, doi:10.1029/ 2006JC003836.

Flocco, D., D. L. Feltham, and A. K. Turner (2010), Incorporation of a physically based melt pond scheme into the sea ice component of a climate model. *J. Geophys. Res., 115*, C08012, doi:10.1029/ 2009JC005568.

Flocco, D., D. *Schroeder*, D. L. Feltham, and E. C. Hunke (2012), Impact of melt ponds on Arctic sea ice simulations from 1990 to 2007, *J. Geophys. Res., 117*, doi:10.1029/2012JC008195.

Flocco, D., D.L. Feltham, E. Bailey, and D. Schroeder (2015), The refreezing of melt ponds on Arctic sea ice, *J. Geophys. Res. - Oceans, 120,* 647–659, doi:10.1002/2014JC010140.

Golden, K.M., H. Eicken, A. L. Heaton, J. Miner, D. J. Pringle, and J. Zhu (2007), Thermal evolution of permeability and microstructure in sea ice. *Geophys. Res. Lett., 34*, L16501, doi:10.1029/2007GL030447.

Grenfell, T. C., and D. K. Perovich (2004), Seasonal and spatial evolution of albedo in a snow-ice-land-ocean environment, *J. Geophys. Res., 109*, C01001, doi:10.1029/2003JC001866.

Haas, C., J. Lobach, S. Hendricks, L. Rabenstein, and A. Pfaffling (2009), Helicopter-borne measurements of sea ice thickness, using a small and lightweight, digital EM system. *Journal of Applied Geophysics 67(3)*: 234–241.

Han, H., Im, J., Kim, M., Sim, S., Kim, J., Kim, D. J., and Kang, S. H. (2016), Retrieval of melt ponds on arctic multiyear sea ice in summer from Terrasar-X dual-polarization data using machine learning approaches: A case study in the Chukchi sea with mid-incidence angle data. *Remote Sensing, 8(57),* 1–23. https://doi.org/10.3390/rs8010057.

Hassol, S.J. (2004), *Impacts of a Warming Arctic: Arctic Climate Impact Assessment*, 139 pp., Cambridge Univ. Press, New York.

Hibler, W.D. III (1980), Modeling a variable thickness sea ice cover. *Mon. Wea. Rev., 1,* 943–1973.

Holland, M. M., D. A. Bailey, B. P. Briegleb, B. Light, and E. Hunke (2012), Improved sea ice shortwave radiation physics in CCSM4: The impact of melt ponds and aerosols on Arctic sea ice. *J. Climate*, *25*, 1413–1430.

Hunke, E.C., D. A. Hebert, and O. Lecomte (2013), Level-ice melt ponds in the Los Alamos Sea Ice Model, CICE. *Ocean Mod., 71*:26–42.

Hunke, E. C., W. H. Lipscomb, A. K. Turner, N. Jeffery, S. Elliott (2015), CICE: The Los Alamos Sea Ice Model Documentation and Software User's Manual Version 5.1, LA-CC-06-012.

Johnson, M., A. Proshutinsky, Y. Aksenov, A.T. Nguyen, R. Lindsay, C. Haas, J. Zhang, N. Diansky, R. Kwok, W. Maslowski, S. Hakkine, I. Ashik, and Beverly de Cuevas (2012), Evaluation of Arctic sea ice thickness simulated by Arctic Ocean Model Intercomparison Project models, *J. Geophy. Res*., *117*, C00D13, doi: 10.1029/2011JC007257.

Kalnay, E., et al. (1996), The NCEP/NCAR 40-year reanalysis project, *Bull. Amer. Meteorol. Soc.*, *77*, 437–471.

Kwok, R. (2007), Near zero replenishment of the Arctic multiyear sea ice cover at the end of 2005 summer, *Geophys. Res Lett.*, *34*, L05501, doi:10.1029/2006GL028737.

Kwok, R. and N. Untersteiner (2011), New High-Resolution Images of Summer Arctic Sea Ice, *Eos Trans. AGU, 92(7)*, 53.

Krishfield, R. A., A. Proshutinsky, K. Tateyama, W. J. Williams, E. C. Carmack, F. A. McLaughlin, *and* M.-L. Timmermans (2014), Deterioration of perennial sea ice in the Beaufort Gyre from 2003 to 2012 and its impact on the oceanic freshwater cycle, *J. Geophys. Res. Oceans*, *119*, 1271–1305, *doi:*10.1002/2013JC008999.

Kurtz, N. T., S. L. Farrell, M. Studinger, N. Galin, J. P. Harbeck, R. Lindsay, V. D. Onana, B. Panzer, and J. G. Sonntag (2013), Sea ice thickness, freeboard, and snow depth products from Operation IceBridge airborne data. *The Cryosphere 7*: 1035–1056. doi:10.5194/tc-7-1035-2013.

Light, B., T. C. Grenfell, and D. K. Perovich (2008), Transmission and absorption of solar radiation by Arctic sea ice during the melt season, *J. Geophys. Res., 113*, C03023, doi:10.1029/2006JC003977.

Light, B., D. K. Perovich, M. A. Webster, C. Polashenski, and R. Dadic (2015), Optical properties of melting first-year Arctic sea ice, *J. Geophys. Res. Oceans, 120*, 7657–7675, doi:10.1002/2015JC011163.

Lindsay, R. W. and J. Zhang (2006), Assimilation of ice concentration in an ice-ocean model, *J. Atmos. Ocean. Tech*., 23, 742–749.

Lindsay, R. W. (2010), Unified Sea Ice Thickness Climate Data Record, Polar Science Center, Applied Physics Laboratory, University of Washington, psc.apl.washington.edu/sea_ice_cdr, digital media.

Lindsay, R. (2013), Unified Sea Ice Thickness Climate Data Record Collection Spanning 1947-2012. Boulder, Colorado USA: National Snow and Ice Data Center. *http://dx.doi.org/10.7265/N5D50JXV.*

Lindsay, R., M. Wensnahan, A. Schweiger, and J. Zhang (2014), Evaluation of seven different atmospheric reanalysis products in the Arctic, *J. Climate*, *27*, 2588–2606, doi: http://dx.doi.org/10.1175/JCLI-D-13-00014.s1.

Lindsay, R., and A. Schweiger (2015), Arctic sea ice loss determined using subsurface, aircraft, and satellite observations, *Cryosphere*, *9*, 269–283, doi:10.5194/tc-9-269-2015.

Liu, J., M. Song, R. M. Horton and Y. Hu (2015), Revisiting the potential of melt pond fraction as a predictor for the seasonal Arctic sea ice extent minimum, *Environ. Res. Lett., 10(5)*, 05401.

Lowry, K., G.L. van Dijken, and K.R. Arrigo (2014), Evidence of under-ice phytoplankton blooms in the Chukchi Sea from 1998 to 2012, *Deep-Sea Research II*, http://dx.doi.org/10.1016/j.dsr2.2014.03.013.

Lüpkes, C., V. M. Gryanik, A. Rösel, G. Birnbaum, and L. Kaleschke (2013), Effect of sea ice morphology during Arctic summer on atmospheric drag coefficients used in climate models, *Geophys. Res. Lett.*, *40*, 446–451, doi: 10.1002/grl.50081.

Lüthje, M., D. L. Feltham, P. D. Taylor, *and* M. G. Worster (2006), Modeling the summertime evolution of sea-ice melt ponds, *J. Geophys. Res.*, *111*, C02001, doi:10.1029/2004JC002818.

Manda, A., N. Hirose, and T. Yanagi (2005), Feasible method for the assimilation of satellite-derived SST with an ocean circulation model, *J. Atmos. Ocean. Tech*., *22*(6), 746–756, doi:10.1175/JTECH1744.1.

Maslanik, J. ., C. Fowler, J. Stroeve, S. Drobot, J. Zwally, D. Yi, and W. Emery (2007), A younger, thinner Arctic ice cover: Increased potential for rapid, extensive sea-ice loss, *Geophys. Res. Lett.*, *34*, L24501, doi: 10.1029/2007GL032043.

Maykut, G. A. (1982), Large-scale heat exchange and ice production in the central Arctic. *J. Geophys. Res.*, *87*, 7971–7984.

Meier, W.N. and others (2014), Arctic sea ice in transformation: A review of recent observed changes and impacts on biology and human activity, *Rev. Geophys.*, *51*, doi:10.1002/2013RG000431.

Melling, H., and D. A. Riedel (2008), Ice Draft and Ice Velocity Data in the Beaufort Sea, 1990–2003. Boulder, Colorado USA, edited, National Snow and Ice Data Center.

Morassutti, M. P., and E. F. LeDrew (1996), Albedo and depth of melt ponds on sea ice, *Int. J. Climatol.*, *16*, 817–838.

Nghiem, S.V., I.G. Rigor, D.K. Perovich, P. Clemente-Colon, and J.W. Weatherly (2007), Rapid reduction of Arctic perennial sea ice, *Geophys. Res. Lett.*, *34*, L19504, doi:10.1029/2007GL031138.

Nicolaus, M., C. Katlein, J. Maslanik, and S. Hendricks (2012), Changes in Arctic sea ice result in increasing light transmittance and absorption, Geophys. Res. Lett., 39, L24501, doi:10.1029/2012GL053738.

Pedersen, C. A., E. Roeckner, M. Lüthje, and J.-G. Winther (2009), A new sea ice albedo scheme including melt ponds for ECHAM5 general circulation model. *J. Geophys. Res.*, *114*, D08101, doi:10.1029/2008JD010440.

Perovich, D. K. (1996), The optical properties of sea ice, U. S. Cold Reg. Res. and Eng. Lab. *Monogr. 96-1*, 25 pp., Hanover, N. H., May 1996.

Perovich, D. K., T. C. Grenfell, B. Light, and P. V. Hobbs (2002), Seasonal evolution of the albedo of multiyear Arctic sea ice, *J. Geophys. Res., 107(C10)*, 8044, doi:10.1029/2000JC000438.

Perovich, D. K., B. Light, H. Eicken, K. F. Jones, K. Runciman, and S. V. Nghiem (2007), Increasing solar heating of the Arctic Ocean and adjacent seas, 1979–2005: Attribution and role in the ice-albedo feedback, *Geophys. Res. Lett., 34,* L19505, doi:10.1029/2007GL031480.

Perovich, D. K., J. A. Richter-Menge, and K. F. Jones (2008), Sunlight, water, and ice: Extreme Arctic sea ice melt during the summer of 2007, *Geophys. Res. Lett., 35*, L11501, doi:10.1029/2008GL034007.

Polashenski, C., D. Perovich, and Z. Courville (2012), The mechanisms of sea ice melt pond formation and evolution, *J. Geophys. Res.*, *117*, C01001, doi:10.1029/2011JC00723.

Rampal, P., J. Weiss, and D. Marsan (2009), Positive trend in the mean speed and deformation rate of Arctic sea ice, 1979–2007, *J. Geophys. Res.*, *114*, doi:10.1029/2008JC005066.

Richter-Menge, J., J. E. Overland, and J. T. Mathis, Eds. (2016), Arctic Report Card 2016, http://www.arctic.noaa.gov/Report-Card.

Roeckner, E., T. Mauritsen, M. Esch, *and* R. Brokopf (2012), Impact of melt ponds on Arctic sea ice in past and future climates as simulated by MPI-ESM, *J. Adv. Model. Earth Syst.*, *4*, M00A02, doi:10.1029/2012MS000157.

Rösel, A., and L. Kaleschke (2012), Exceptional melt pond occurrence in the years 2007 and 2011 on the Arctic sea ice revealed from MODIS satellite data, *J. Geophys. Res.*, *117*, C05018, doi:10.1029/2011JC007869.

Rösel, A., L. Kaleschke, and G. Birnbaum (2012), Melt ponds on Arctic sea ice determined from MODIS satellite data using an artificial neuronal network, *Cryosphere*, *6*, 1–19, *doi:*10.5194/tc-6-1-2012.

Rothrock, D. A., D. B. Percival, and M. Wensnahan (2008), The decline in arctic sea-ice thickness: Separating the spatial, annual, and interannual variability in a quarter century of submarine data, *J. Geophys. Res.*, *113*(C5).

Saha, S., and others (2010), The NCEP Climate Forecast System Reanalysis. *Bull. Amer. Meteor. Soc.*, *91*, 1015–1057.

Saha, S., and others (2014), The NCEP climate forecast system version 2, *J. Climate*, *27*, 2185–2208.

Santer, B.D., T.M. Wigley, J.S. Boyle, D.J. Gaffen, J.J. Hnilo, D. Nychka, D.E. Parker, and K.E. Taylor (2000), Statistical significance of trends and trend differences in layer-average atmospheric temperature time series, *J. Geophys. Res.*, *105*, 7337–7356.

Schröder, D., D. L. Feltham, D. Flocco, and M. Tsamados (2014), September Arctic sea-ice minimum predicted by spring melt-pond fraction, *Nat. Clim. Change*, *4*(*5*), 353–357, doi:10.1038/nclimate2203.

Schweiger, A., and J. Zhang (2015), Accuracy of short-term sea ice drift forecasts using a coupled ice-ocean model, *J. Geophys. Res. Oceans*, *120*, doi:10.1002/2015JC011237.

Skyllingstad, E. D., and C. A. Paulson (2007), A numerical study of melt ponds, *J. Geophys. Res.*, *112*, C08015, doi:10.1029/2006JC003729.

Skyllingstad, E. D., C. A. Paulson, and D. K. Perovich (2009), Simulation of melt pond evolution on level ice, *J. Geophys. Res.*, *114*, C12019, doi:10.1029/2009JC005363.

Smith, R. D., J. K. Dukowicz and R. C. Malone (1992), Parallel Ocean General-Circulation Modeling, *Physica D 60(1-4)*, 38–61.

Steele, M., J. Zhang, and W. Ermold (2010), Mechanisms of summertime upper Arctic Ocean warming and the effect on sea ice melt, *J. Geophy. Res.*, *115*, C11004, doi: 10.1029/2009JC005849.

Thorndike, A.S., D.A. Rothrock, G.A. Maykut, and R. Colony (1975), The thickness distribution of sea ice. *J. Geophys. Res.*, *80*, 4501–4513.

Tsamados, M., D. Feltham, A. Petty, D. Schroeder, and D. Flocco (2015), Processes controlling surface, bottom and lateral melt of Arctic sea ice in a state of the art sea ice model. *Phil. Trans. R. Soc. A 373*, 20140167.

Webster, M. A., I. G. Rigor, S. V. Nghiem, N. T. Kurtz, S. L. Farrell, D. K. Perovich, and M. Sturm (2014), Interdecadal changes in snow depth on Arctic sea ice. *J. Geophys. Res. Oceans*, *119*, 5395–5406, doi:10.1002/2014JC009985.

Webster, M. A., Rigor, I. G., Perovich, D. K., Richter-Menge, J. A., Polashenski, C. M., & Light, B. (2015). Seasonal evolution of melt ponds on Arctic sea ice. *Journal of Geophysical Research-Oceans, 120*(9), 5968–5982. doi:10.1002/2015jc011030.

Witte, H., and E. Fahrbach (2005), AWI Moored ULS Data, Greenland Sea and Fram Strait, 1991-2002, edited, National Snow and Ice Data Center.

Zhang, J., and D.A. Rothrock (2001), A thickness and enthalpy distribution sea-ice model, *J. Phys. Oceanogr*., *31*, 2986–3001.

Zhang, J., and D.A. Rothrock (2003), Modeling global sea ice with a thickness and enthalpy distribution model in generalized curvilinear coordinates, *Mon. Wea. Rev*., *131(5)*, 681–697.

Zhang, J., R.W. Lindsay, M. Steele, and A. Schweiger (2008), What drove the dramatic retreat of Arctic sea ice during summer 2007? *Geophys. Res. Lett.*, *35*, L11505, doi:10.1029/2008GL034005.

Zhang, J., R. Lindsay, A. Schweiger, and I. Rigor (2012), Recent changes in the dynamic properties of declining Arctic sea ice: A model study, *Geophys. Res. Lett.*, *39*, L20503, doi:10.1029/2012GL053545.

Zhang, J., M. Steele, K. Runciman, S. Dewey, J. Morison, C. Lee, L. Rainville, S. Cole, R. Krishfield, M.-L. Timmermans, and J. Toole (2016), The Beaufort Gyre intensification and stabilization: A model-observation synthesis, *J. Geophys. Res. Oceans*, *121*, doi:10.1002/2016JC01219.

Table 1. Albedo (broadband) parameters for different surface conditions.

Surface condition	Albedo
Freezing snow	0.80
Melting snow	0.70
Freezing bare ice	0.75
Melting bare ice	0.58
Open water	0.10

Table 2. 1979–2016 mean and linear trends for variables shown and described in Figures 4 and 12. Bold numbers exceed the 95% confidence level when tested in a way that accounts for temporal autocorrelation. The unit for the relative trend in column four (Trend / |Mean| × 100%) is $\%yr^{-1}$.

	Mean	Trend	Trend / |Mean| × 100 %	Unit of Trend
Ice volume (Jun–Aug mean)	19.78	**–0.25**	**–1.26**	10^3 km^3 yr^{-1}
Ice area (Jun–Aug mean)	6.00	**–0.053**	**–0.88**	10^6 km^2 yr^{-1}
MP volume (Jun–Aug mean)	1.07	**–0.015**	**–1.40**	10^3 km^3 yr^{-1}
MP area (Jun–Aug mean)	1.49	**–0. 014**	**–0.93**	10^6 km^2 yr^{-1}
Total ice melt (per unit area) (Jun–Aug mean)	0.60	**0.0021**	**0.35**	m mon^{-1} yr^{-1}
Top ice melt (per unit area) (Jun–Aug mean)	0.44	–0.0010	–0.22	m mon^{-1} yr^{-1}
Bottom & lateral ice melt (Jun–Aug mean)	0.17	**0.0031**	**1.82**	m mon^{-1} yr^{-1}
Snow volume (Apr–Jun mean)	2.23	**–0.022**	**–0.98**	10^3 km^3 yr^{-1}
Snow melt (May–Jul mean)	0.093	**–0.00062**	**–0.66**	m mon^{-1} yr^{-1}
MP volume per unit ice area (Jun–Aug mean)	0.21	–0.00065	–0.31	m yr^{-1}
MP fraction per unit ice area (Jun–Aug mean)	0.27	–0.00017	–0.063	Fraction yr^{-1}
Top ice melt per unit ice area (Jun–Aug mean)	0.81	0.00086	0.11	m mon^{-1} yr^{-1}
MP water loss per unit ice area (Jun–Aug mean)	0.87	0.00187	0.21	m mon^{-1} yr^{-1}

Table 3. Numerical parameters used in the control (CNTL) and sensitivity (SEN1, SEN2, and NoMP) simulations, including the drainage scaling factor d_p in (4) and the ice thickness scaling factor C_h in (12).

Model simulation	d_p	C_h
CNTL	0.015	0.75
SEN1	0.025	0.75
SEN2	0.015	1/h*
NoMP	–	–

* h is ice thickness.

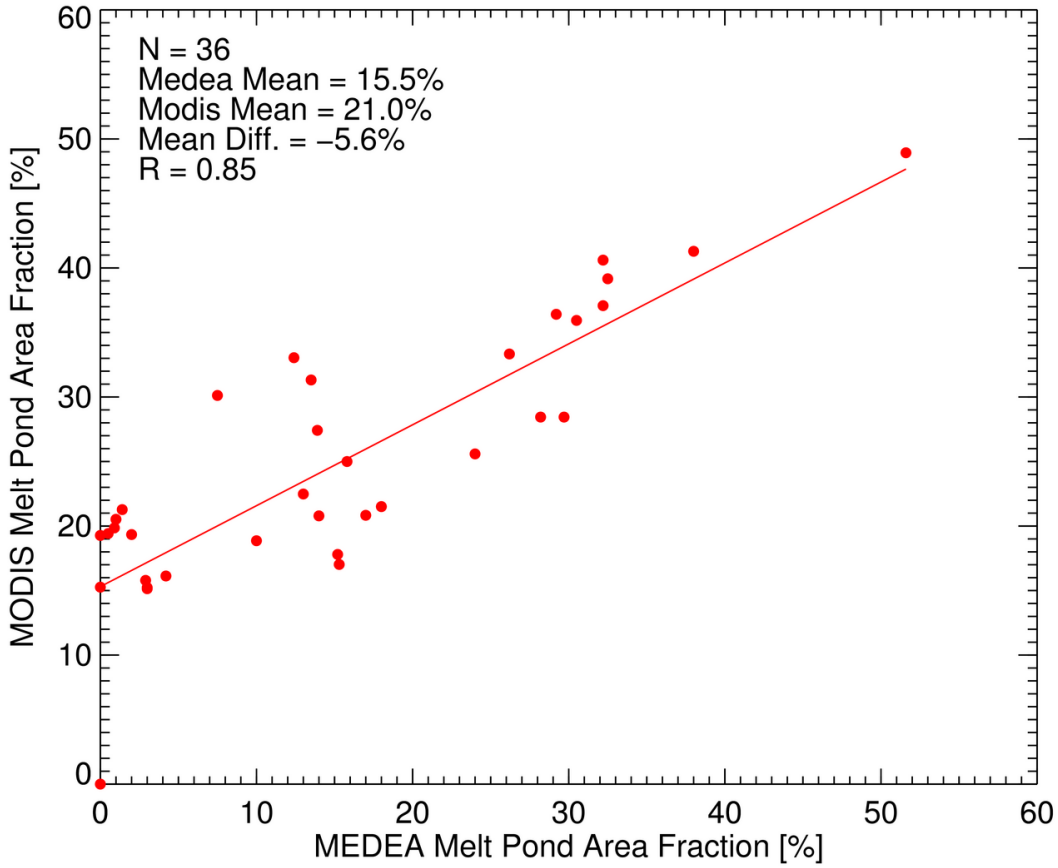

Figure 1. A comparison between MODIS observations of MP area fraction and corresponding MEDEA observations. The number of total observation points (N), MODIS and MEDEA mean values, mean difference, and MODIS–MEDEA correlation (R) are listed.

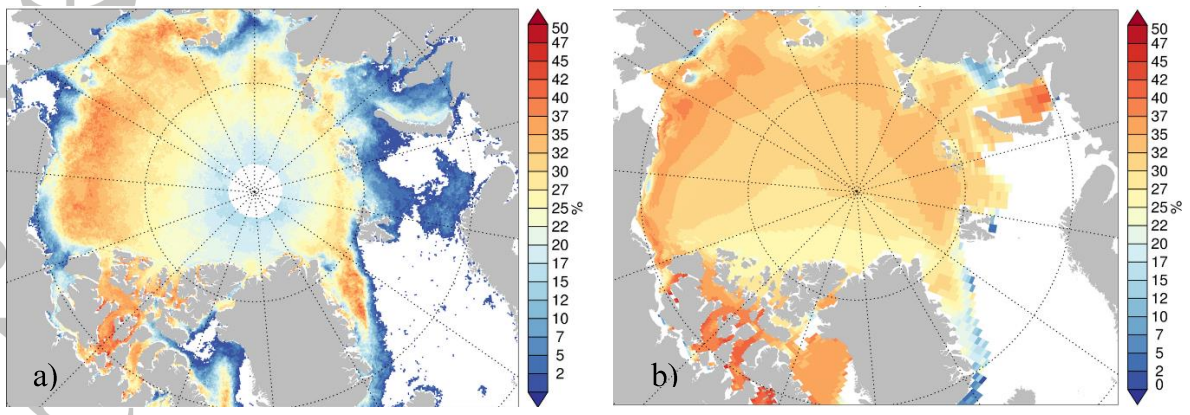

Figure 2. July 2000–2011 mean MP area fraction (%) derived from MODIS images (a) and simulated by MIZMAS (b).

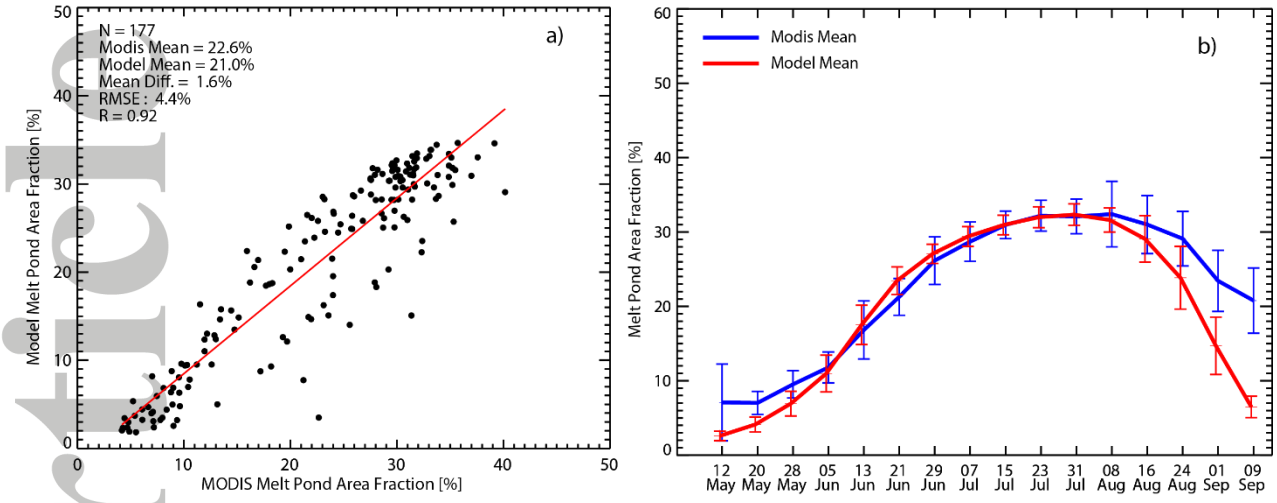

Figure 3. (a) A comparison of model simulated MP area fraction with available MODIS observations, averaged weekly over the whole Arctic Ocean (excluding the region near the North Pole where there is no MODIS data, see Figure 2a) for May through August of 2000–2011; the number of total observation points (N), model and observation mean values, mean model bias, root-mean-squared error (RMSE), and model–observation correlation (R) are listed. (b) 2000–2011 mean and standard deviation (vertical lines) of seasonal evolution of model simulated and MODIS observed MP area fraction, averaged weekly over the Arctic Ocean.

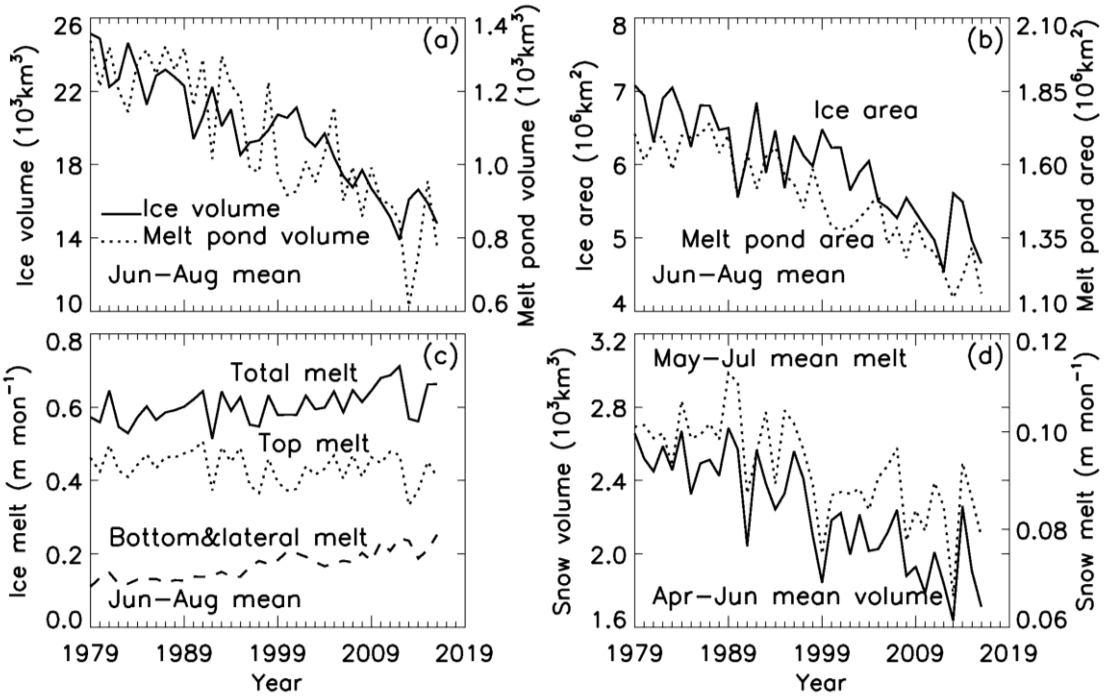

Figure 4. Simulated June–August mean sea ice volume (solid line) and MP volume (dotted line) (a), sea ice area (solid line) and MP area (dotted line) (b), and sea ice top (solid line), bottom and lateral (dashed line), and total melt (dotted line) (c), and simulated April–June mean snow volume (solid line) and May–July mean snow melt (dotted line) (d), averaged over the Arctic Ocean. MP volume is the integration of MP volume per unit area defined as $V_p = (\rho_i/\rho_w) \int_0^\infty g_p(h)hdh$ (see section 3) over the Arctic. Note that the snow volume and melt in (d) are not averaged over the June–August period because snow has mostly melted by July (see Figure 5d).

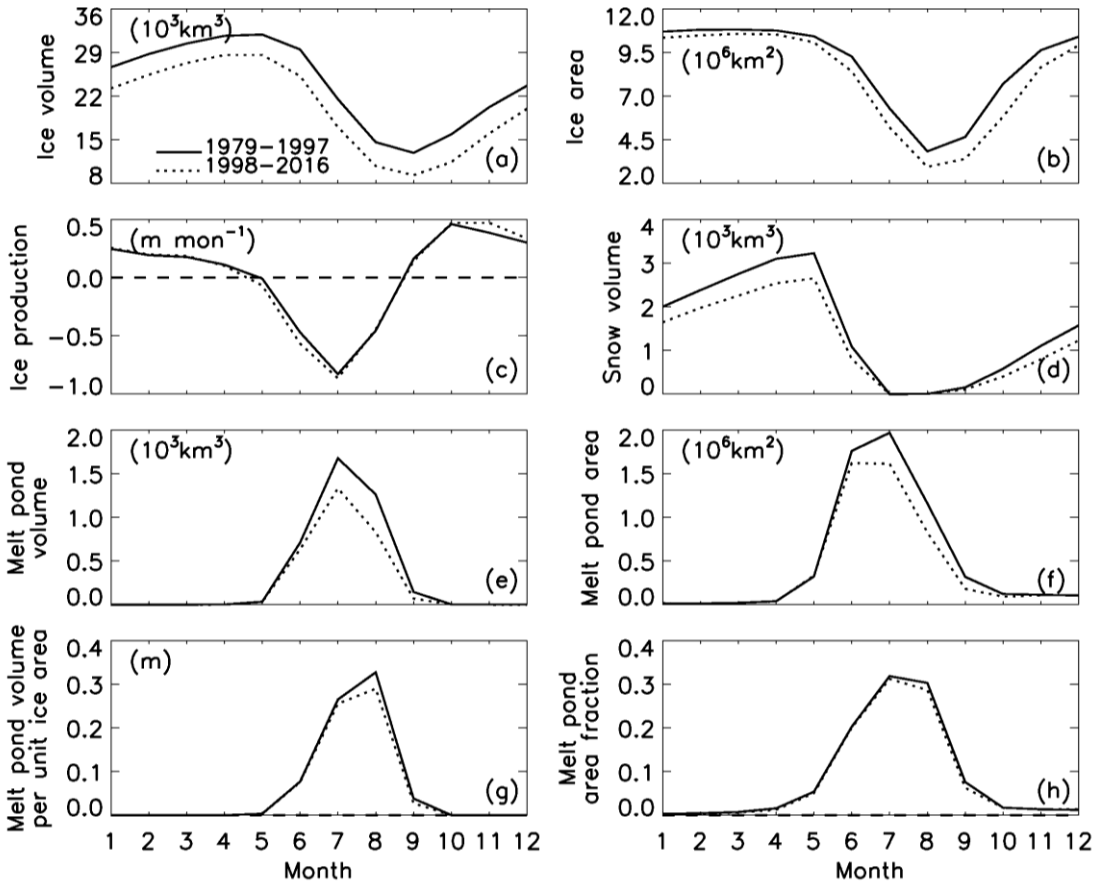

Figure 5. Simulated seasonal evolution of sea ice volume (a), area (b), and production (c), snow volume (d), MP volume (e) and area (f), MP volume per unit ice area (g), and MP fraction per unit ice area or MP area fraction (h), integrated or averaged over the Arctic for the periods 1979–1997 (solid line) and 1998–2016 (dotted line).

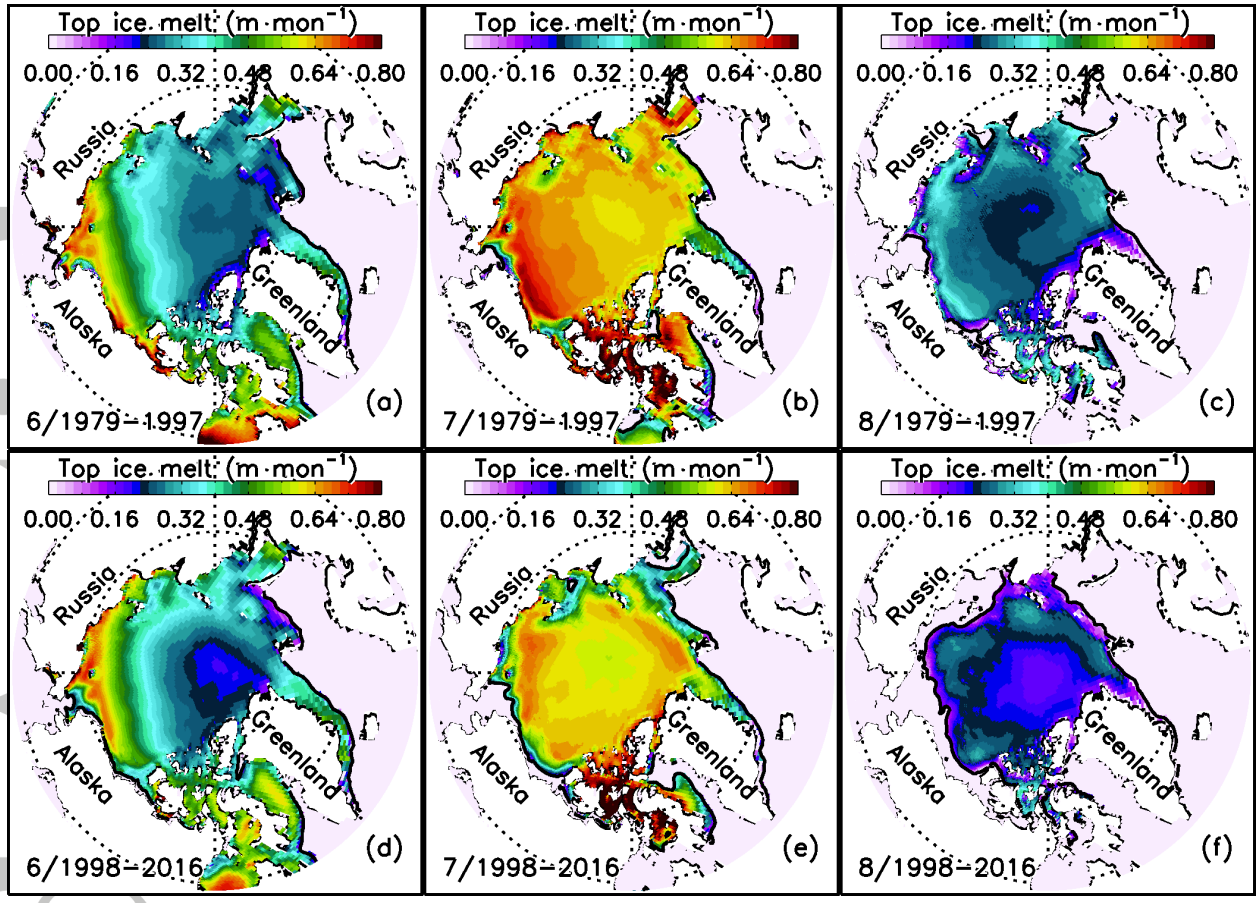

Figure 6. Simulated top ice melt (per unit area) for June (a, d), July (b, e), and August (c, f) averaged over the periods 1979–1997 and 1998–2016. Black line represents satellite observed ice edge defined as 0.15 ice concentration.

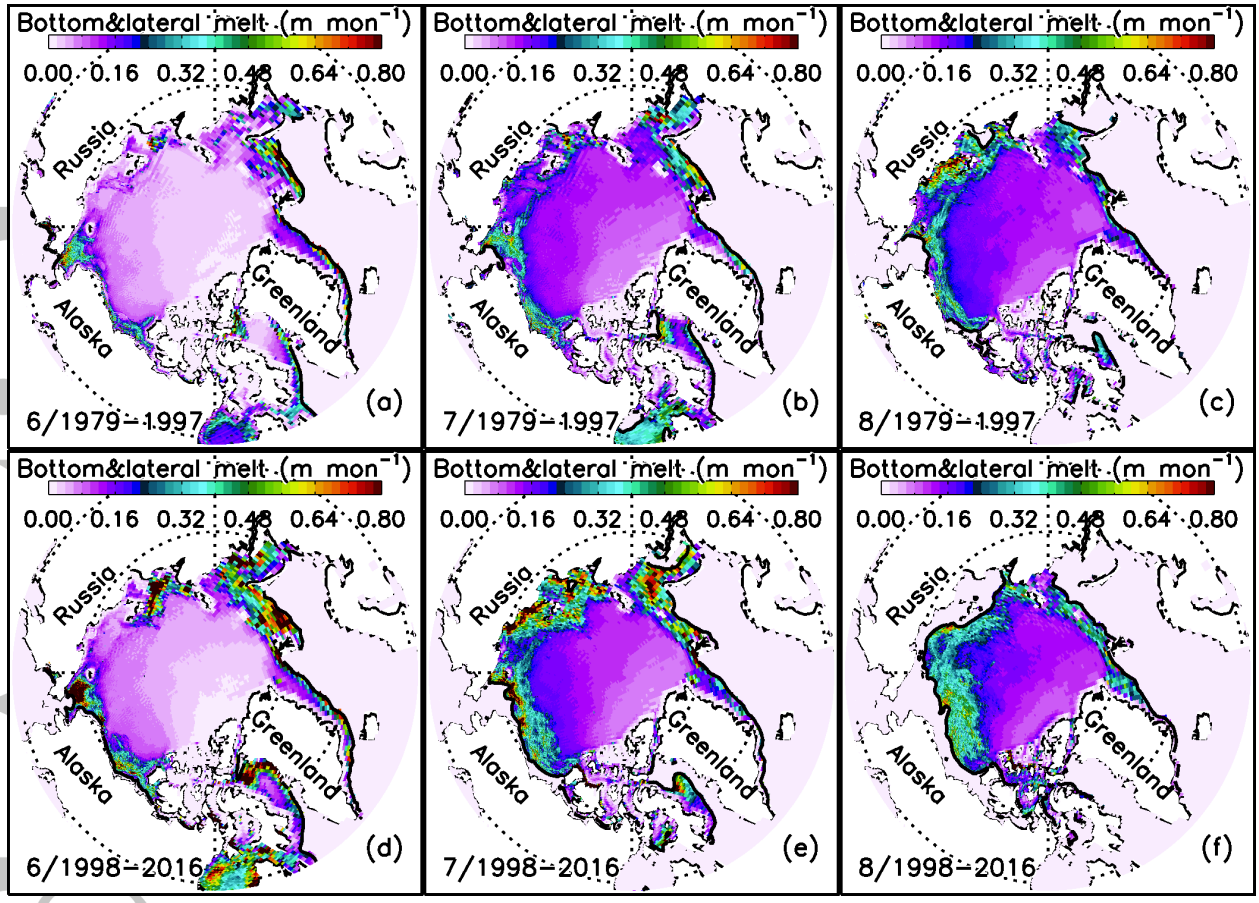

Figure 7. Simulated combined bottom and lateral melt (per unit area) for June (a, d), July (b, e), and August (c, f) averaged over the periods 1979–1997 and 1998–2016.

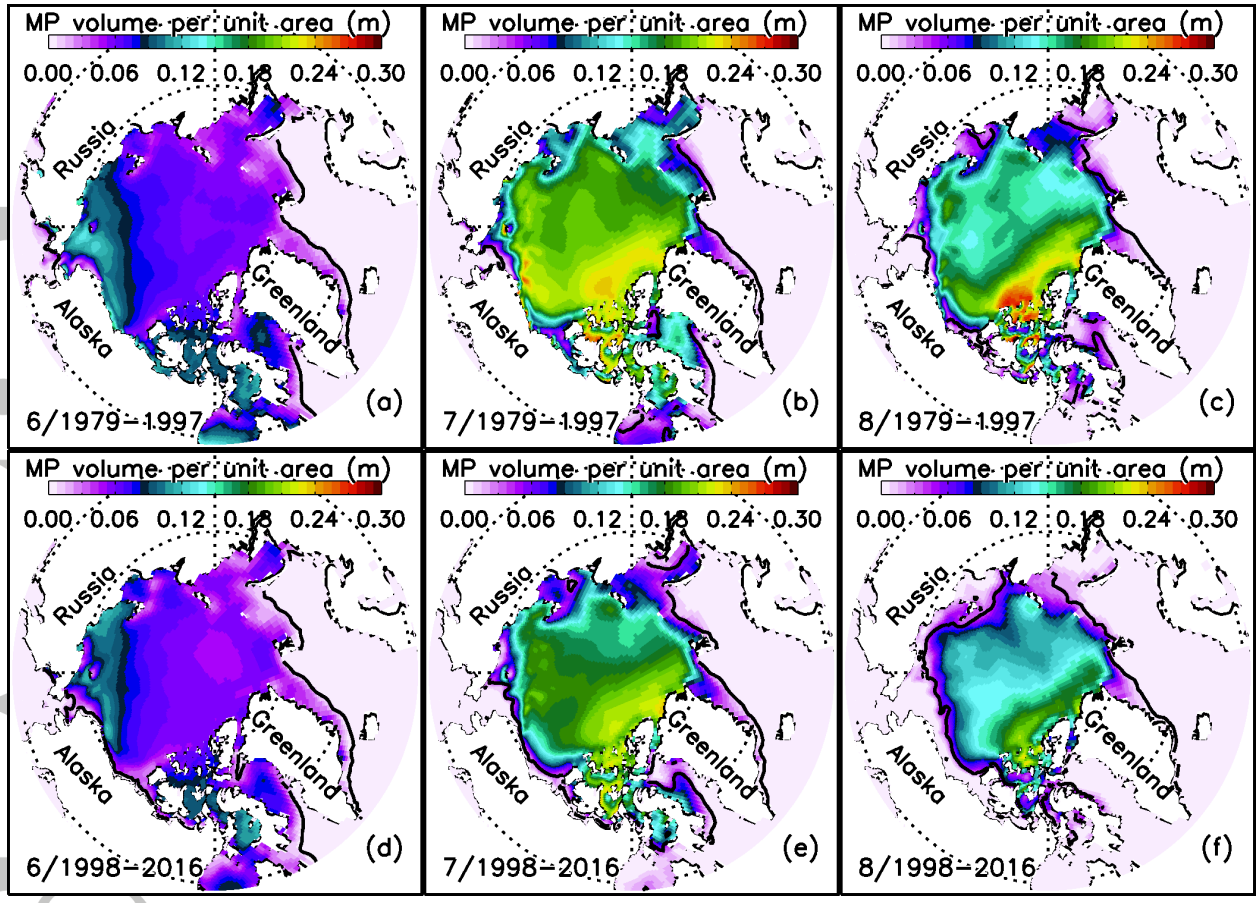

Figure 8. Simulated MP volume per unit area (m) for June (a, d), July (b, e), and August (c, f) averaged over the periods 1979–1997 and 1998–2016. MP volume per unit area is defined as $V_p = (\rho_i/\rho_w) \int_0^\infty g_p(h)hdh$ with units of meter (also see Figure 4 caption).

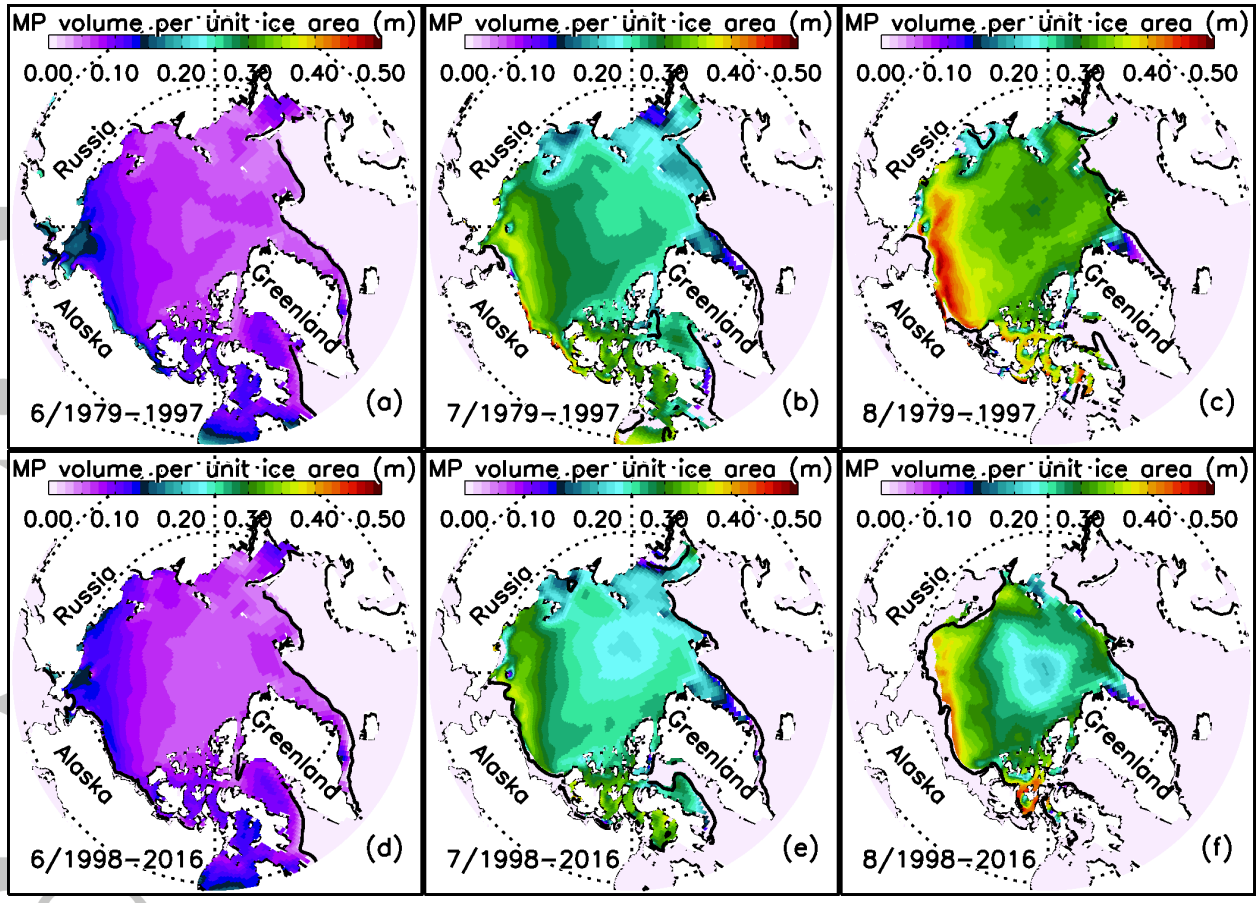

Figure 9. Same as Figure 8 but for MP volume per unit ice area. MP volume per unit ice area is defined here as MP volume per unit area (V_p) divided by ice concentration and thus represents actual MP volume on ice without including open water area.

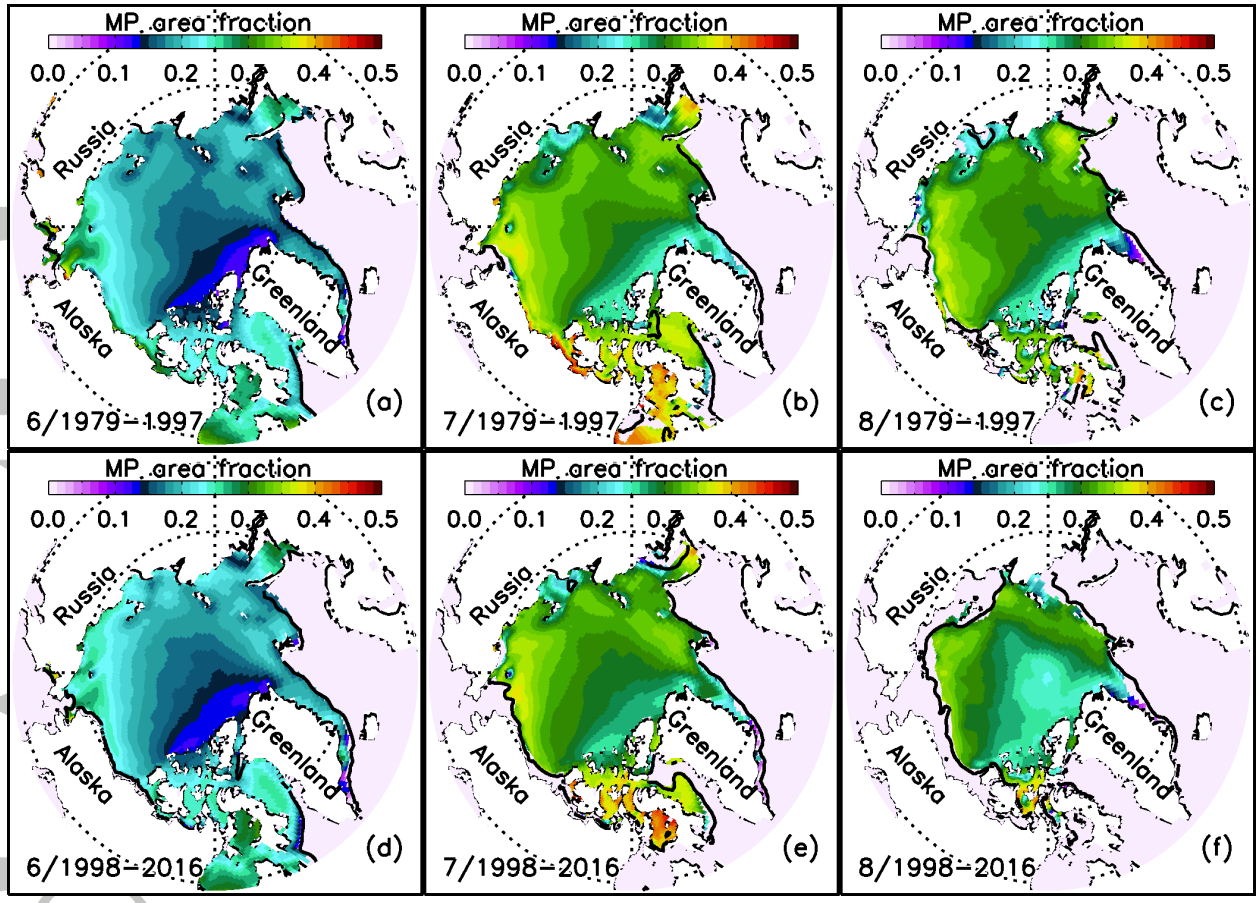

Figure 10. Simulated MP area fraction for June (a, d), July (b, e), and August (c, f) averaged over the periods 1979–1997 and 1998–2016.

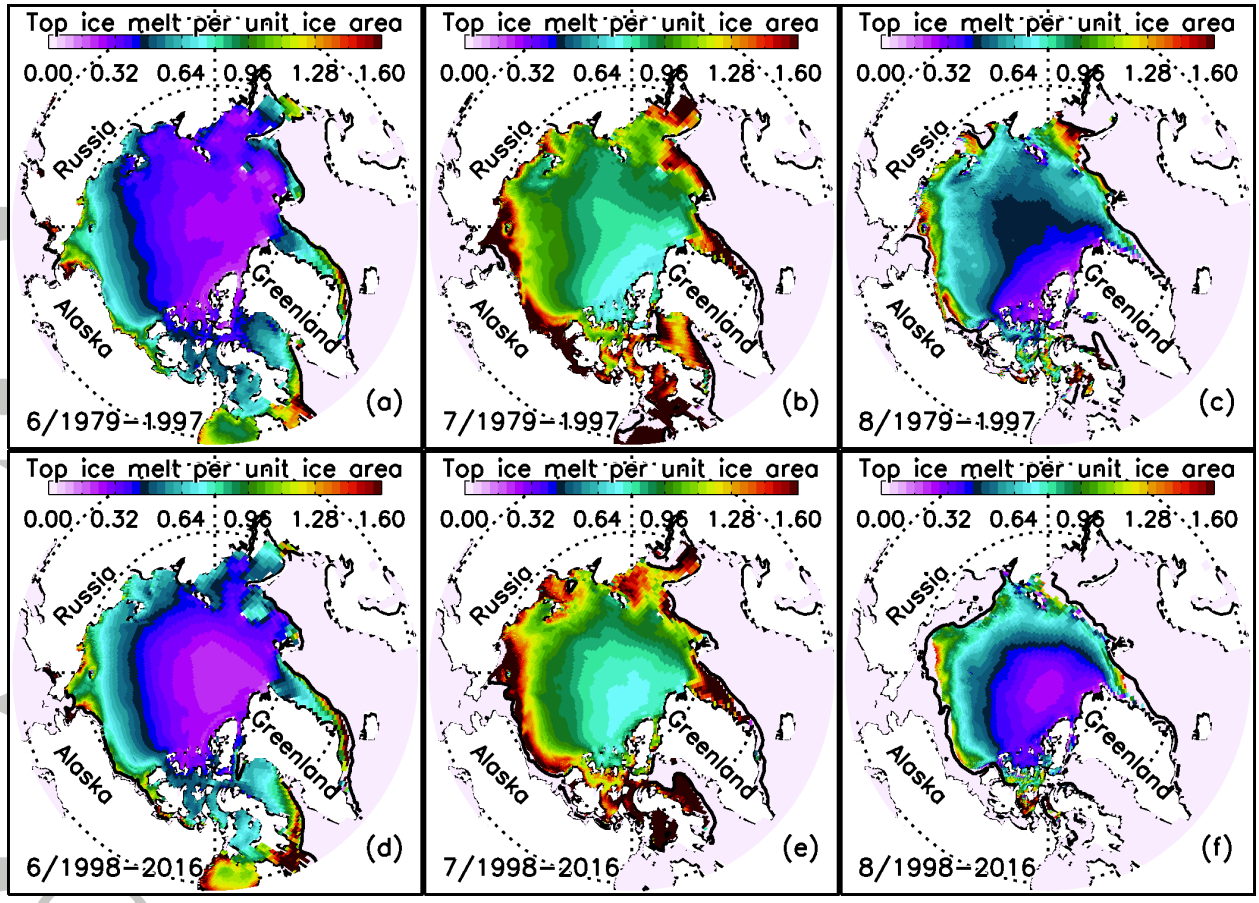

Figure 11. Simulated top ice melt per unit ice area (m mon^{-1}) for June (a, d), July (b, e), and August (c, f) averaged over the periods 1979–1997 and 1998–2016. Top ice melt per unit ice area is defined here as the top ice melt per unit area (shown in Figure 6) divided by ice concentration and thus represents actual top ice melt on ice.

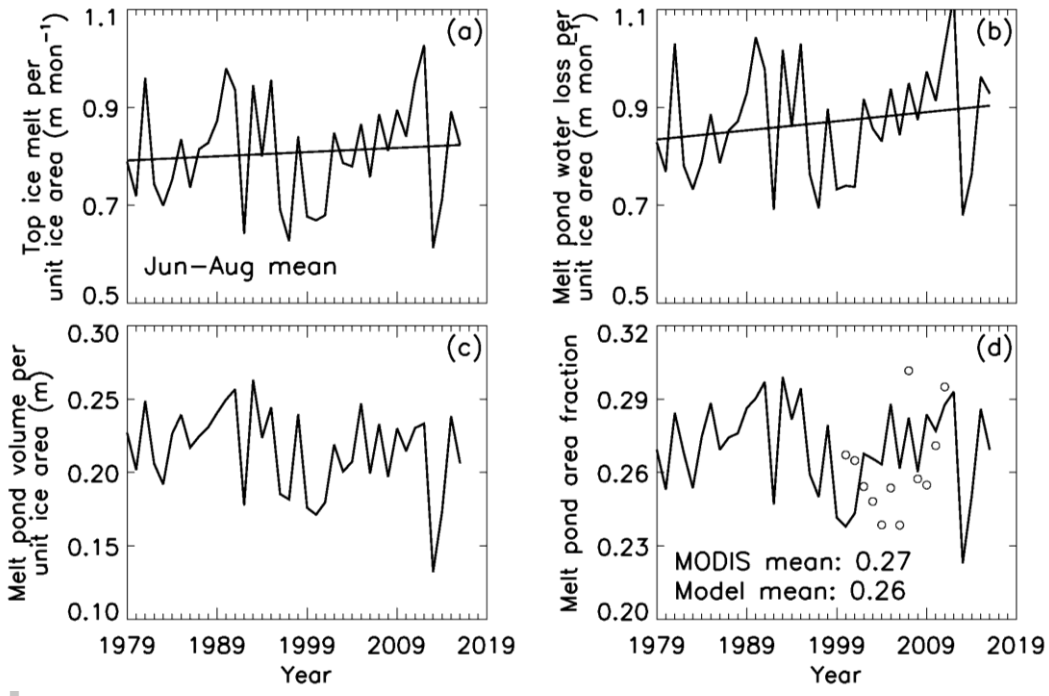

Figure 12. Simulated June–August mean top ice melt per unit ice area (a), MP water loss per unit ice area (b), and MP volume per unit ice area (c) and area fraction (d), averaged over the Arctic Ocean. Here MP water loss is defined as the combination of MP water drainage due to ice porosity (*D*) and ice ridging [see (3)]. Included in (d) is the corresponding June–August mean MP area fraction derived from MODIS observations (circles) for the period 2000–2011, with the MODIS and model mean over the period listed.

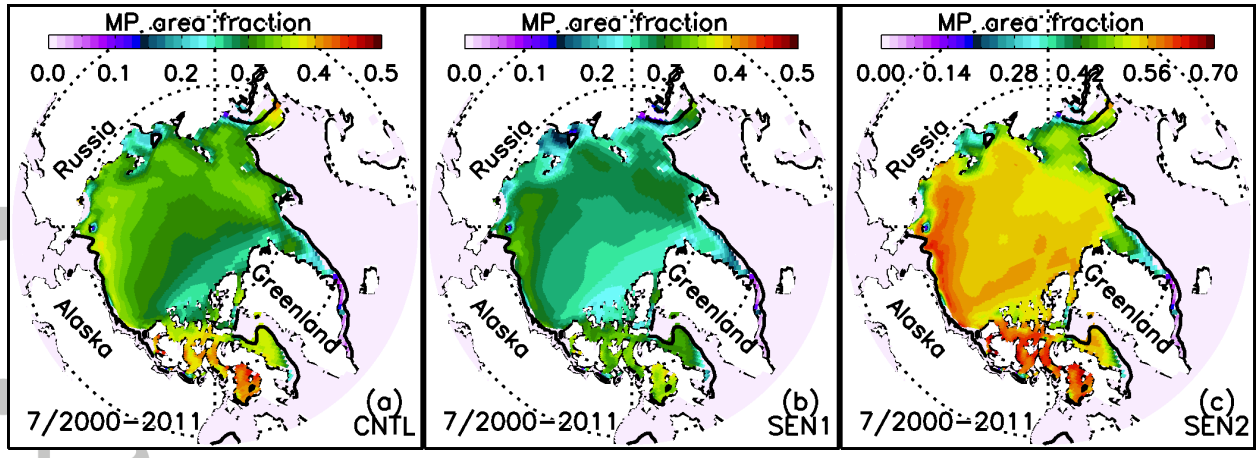

Figure 13. Simulated July 2000–2011 mean MP area fraction for the three model runs with MP incorporated. Note that (a) is a repeat of Figure 2b, with different units and color scales. Color scales in (c) differ from (a) and (b).

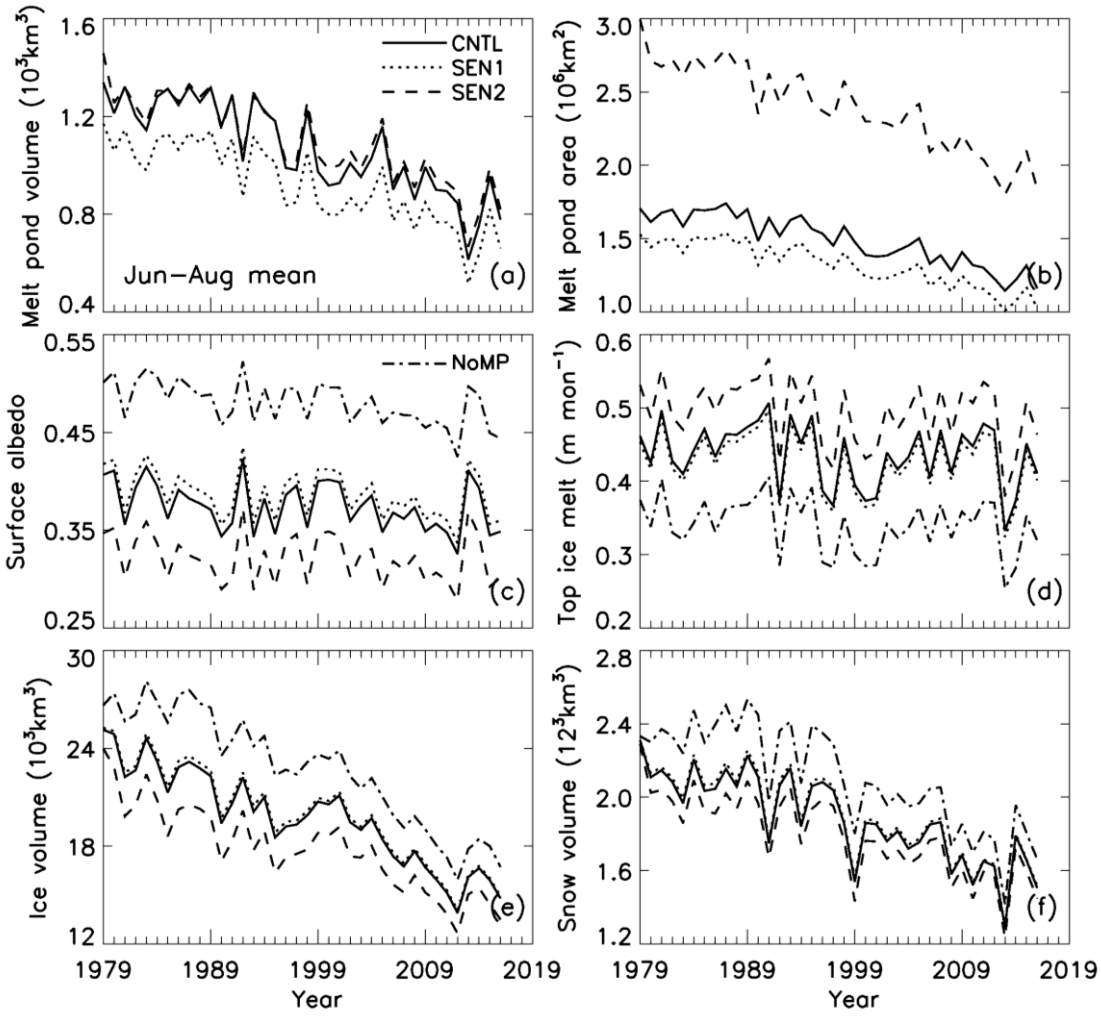

Figure 14. Simulated MP volume (a) and area (b) for the control and two sensitivity runs with MPD incorporated, and mean surface albedo averaged over all surface types (c), top ice melt (per unit area) (d), sea ice volume (e), and snow volume (f) for the control and three sensitivity runs with and without MPD incorporated, integrated or averaged over the Arctic. All variables except snow volume are June–August mean; snow volume is averaged over April–June.